Integrated analysis of surface wave velocity and gravity data for the development of new density-velocity models of the crust and upper mantle in SE Iran

Somayeh Abdollahi, Hermann Zeyen, Vahid Ebrahimzadeh Ardestani, Zaher Hossein Shomali

Journal of Asian Earth Sciences: X 7 (2022) 100101

Contents lists available at ScienceDirect

Journal of Asian Earth Sciences: X

journal homepage: www.sciencedirect.com/journal/journal-of-asian-earth-sciences-x

Integrated analysis of surface wave velocity and gravity data for the development of new density-velocity models of the crust and upper mantle in SE Iran

Somayeh Abdollahi [a,*], Hermann Zeyen [b], Vahid Ebrahimzadeh Ardestani [c], Zaher Hossein Shomali [c]

[a] Institute of Geophysics, Polish Academy of Sciences, ks. Janusza 64, 01–452 Warsaw, Poland
[b] Université Paris-Saclay, CNRS, GEOPS, 91405 Orsay, France
[c] Institute of Geophysics, University of Tehran, P.O. Box 14155-6466, Tehran, Iran

ARTICLE INFO

Keywords:
Simulated Annealing algorithm
Rayleigh wave group velocity data
Shear Velocity
Gravity inversion
Moho Depth
Makran

ABSTRACT

Inversion of Rayleigh wave dispersion curves is challenging due to its nonlinearity and multimodality. In this paper, a Simulated Annealing (SA) algorithm is applied to the nonlinear inversion of fundamental-mode Rayleigh wave group dispersion curves for shear and compressional wave velocities. In our approach, we invert thickness, velocities and densities and their vertical gradients of four layers, sediments, upper-crust, lower-crust and lithospheric mantle.

At first, to determine the efficiency and stability of the method, noise-free and noisy synthetic data sets are inverted. Results from the synthetic data demonstrate that the SA applied to the nonlinear inversion of surface wave data is interesting not only in terms of accuracy but also in terms of the convergence speed. In fact, the SA method is suitable for large-scale optimization problems, especially for those in which a desired global minimum is hidden among many local minima. In a second step, real data in SE Iran are inverted to examine the usage and robustness of the proposed approach on real surface wave data. Then, we applied 3D gravity modeling based on surface wave analysis results to obtain the density structure of each layer. The reason for using both types of data sets is that the gravity anomaly does not have a good vertical resolution and surface wave group velocities are more appropriate for placing layer limits at depth, but they are not very sensitive to density variations. Therefore, the use of gravity data increases the overall resolution of density distribution. Compared with the Shuffle Complex Evolution (SCE) method that was implemented in a previous study, we found out that the SA method is more stable and has less variability of model parameter values in successive tests. In the final step, we reapplied the SA method to invert the fundamental-mode Rayleigh wave group velocities based on the results of gravity modeling. Gravity results, such as thicknesses and densities were used to limit the search space in the SA method.

Our results show that the Moho depth across the Makran subduction zone is increasing from the Oman seafloor (24–30 km) and Makran forearc setting (34–42 km) to the Taftan-Bazman volcanic arc (47–49 km). Also, the results show high shear and compressional velocities under the Gulf of Oman, decreasing to the north of the Makran region. The density image shows an average crustal density with maximum values under the Gulf of Oman, decreasing northward to the Makran region.

1. Introduction

The current configuration of the Iranian plateau has been formed during the Cenozoic, after the closure of Tethys ocean and the continent–continent collision of Arabian and Eurasian plates. This caused active and young tectonic structures within the plateau including the collision in Zagros, and subduction in the Makran. The formation of the Zagros fold belt started after the closure of the Neo-Tethys ocean and the collision of Arabian and Central Iranian plates at the Main Zagros Thrust (MZT in Fig. 1). The beginning of collision is debated among geologists and varies from Late Cretaceous (Berberian, 1981; Agard et al., 2005) to Oligocene–Miocene (Koop and Stoneley, 1982). The Makran subduction

* Corresponding author.
E-mail address: sabdollahi@igf.edu.pl (S. Abdollahi).

https://doi.org/10.1016/j.jaesx.2022.100101
Received 29 May 2021; Received in revised form 7 May 2022; Accepted 19 May 2022
Available online 25 May 2022

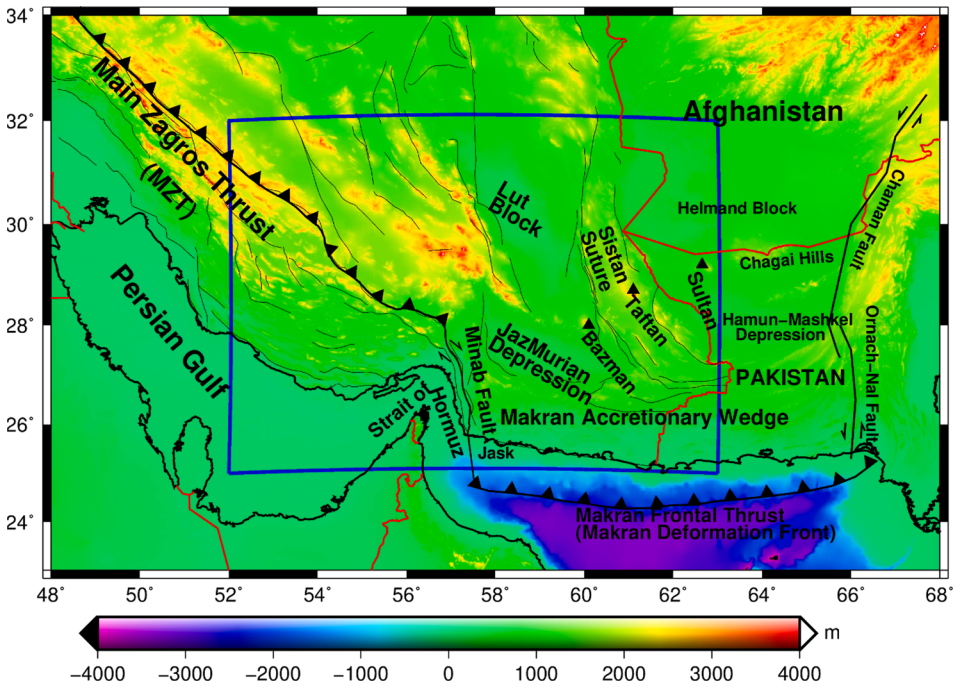

Fig. 1. Main tectonic structures of the study area (blue rectangle) superposed on a topography map www.ngdc.noaa.gov/mgg/global/relief/ETOPO1).

zone extends ~ 1000 km in E-W direction between SE Iran and SW Pakistan and from the Oman Sea to the JazMurian and Mashkel depressions in N-S direction (Fig. 1). The E-W trending Makran is located between two, nearly N-S directed transform fault systems. To the west, the dextral Minab fault separates the Makran subduction zone from the Zagros continent–continent collision zone and to the east, the sinistral Ornach-Nal fault and Chaman fault system separate it from the Indian subcontinent with 300–350 km width. The Makran is a unique subduction zone in terms of its very low subducting angle, wide accretionary prism, and a large distance between its volcanic arc and deformational front (White and Louden, 1982; Penney et al., 2017).

This accretionary complex has been formed by subduction of the oceanic crust of the Arabian Plate under the Eurasian Plate, probably initiated in the Paleocene (Platt et al., 1985; Platt et al., 1988) and accreted since the Eocene (Byrne et al., 1992). The Arabian Plate is being subducted beneath the Eurasian plate along this deformation front (Fig. 1). The Eurasian Plate is dominated by the Lut block to the west and the Helmand block to the east separated by the Sistan Suture Zone which represents the subduction of Neotethys beneath the Helmand Block (Byrne et al., 1992; Berberian and Yeats, 2000). The Sistan oceanic domain is interpreted as a backarc setting or a branch of the Neo-Tethys (Tirrul et al., 1983), formed during the Middle-Late Cretaceous having been closed during the Paleocene–Eocene. Several essentially non-metamorphic ophiolitic remnants are found in the upper plate which represent a backarc setting (Agard et al., 2006; Monié and Agard, 2009).

The Baluchistan volcanic arc, including the Bazman and Taftan volcanoes in Iran and Sultan volcano in Pakistan, is located 400– 600 km away from the deformational front. Onshore, two topographic depressions, the JazMurian and the Hamun-Mashkel, located between the accretionary prism and the Baluchistan volcanoes, are interpreted as forearc basins. These basins are separated by the N-S trending strike-slip Sistan Suture Zone (Fig. 1) which has been suggested to segment the subduction zone into discrete eastern and western zones, based on contrasting levels of seismicity which is higher in the east (Dolati, 2010; Burg, 2018).

The western and eastern parts of the Makran subduction zone have thus different seismic and tectonic characteristics (see Fig. S1 in the Supplementary Material for the seismicity map; Rashidi et al., 2020). The Makran subduction zone is characterized by very little background seismicity, with slightly more activity in the east than in the west, and some clusters of seismicity occurring in the Zendan-Minab fault zone. Large earthquakes were considered to have ruptured the plate boundary; some have been reported in historical times for eastern Makran (Byrne et al., 1992).

Mokhtari et al. (2019) showed that the western Makran is known to be a site of just a few small-magnitude earthquakes. By contrast, large-magnitude and frequent earthquakes characterize the eastern Makran. They suggested three interpretations for the current seismic status of the western Makran: (1) the whole segment is aseismic, (2) subduction does not occur any more along this segment, and (3) the western Makran segment is currently locked and has the potential of producing future large subduction earthquakes. Also, other kinds of evidence such as GPS measurements, have led to speculation that there is a possibly locked seismogenic zone in the western Makran (Byrne et al., 1992; Vernant et al., 2004).

Recent and active deformation in Sistan is dominated by right-lateral strike-slip and thrust faults related to the indentation of Iran by the Arabian shield. The seismic activity in the Taftan-Bazman volcanic arc is quite weak. In 1979, several right-lateral moderate-sized earthquakes occurred in the Sistan Suture Zone. This seismic activity indicates that the Sistan Suture Zone may be defined as a boundary between western and eastern Makran (Byrne et al., 1992). To the east, the distance of the volcanic arc and the fore-arc setting increases, and this suggests that the slab dip decreases eastward (Byrne et al., 1992 Shad Manaman et al., 2011). Eastern Makran has experienced most of its seismic activity in its eastern part, near the Chaman Fault.

The relatively large, 400–600 km gap between the Makran deformational front and the volcanic arc suggests that the subducting plate dips with only 1 – 2° to the north (at ~62.5°E). Shallow subduction is consistent with seismic data (White and Louden, 1982) and earthquake focal mechanisms (e.g. Quittmeyer and Jacob, 1979; Byrne et al., 1992; Alinaghi et al., 2007). Kopp et al. (2000) found that the average dip of the Arabian plate in this area is about 3°. Penney et al. (2017), however, find maximum dips of ~11° in the western Makran, ~9° in the central region, and ~8° in the eastern Makran. The mean dip of the subduction interface in the Makran is thus still an open question.

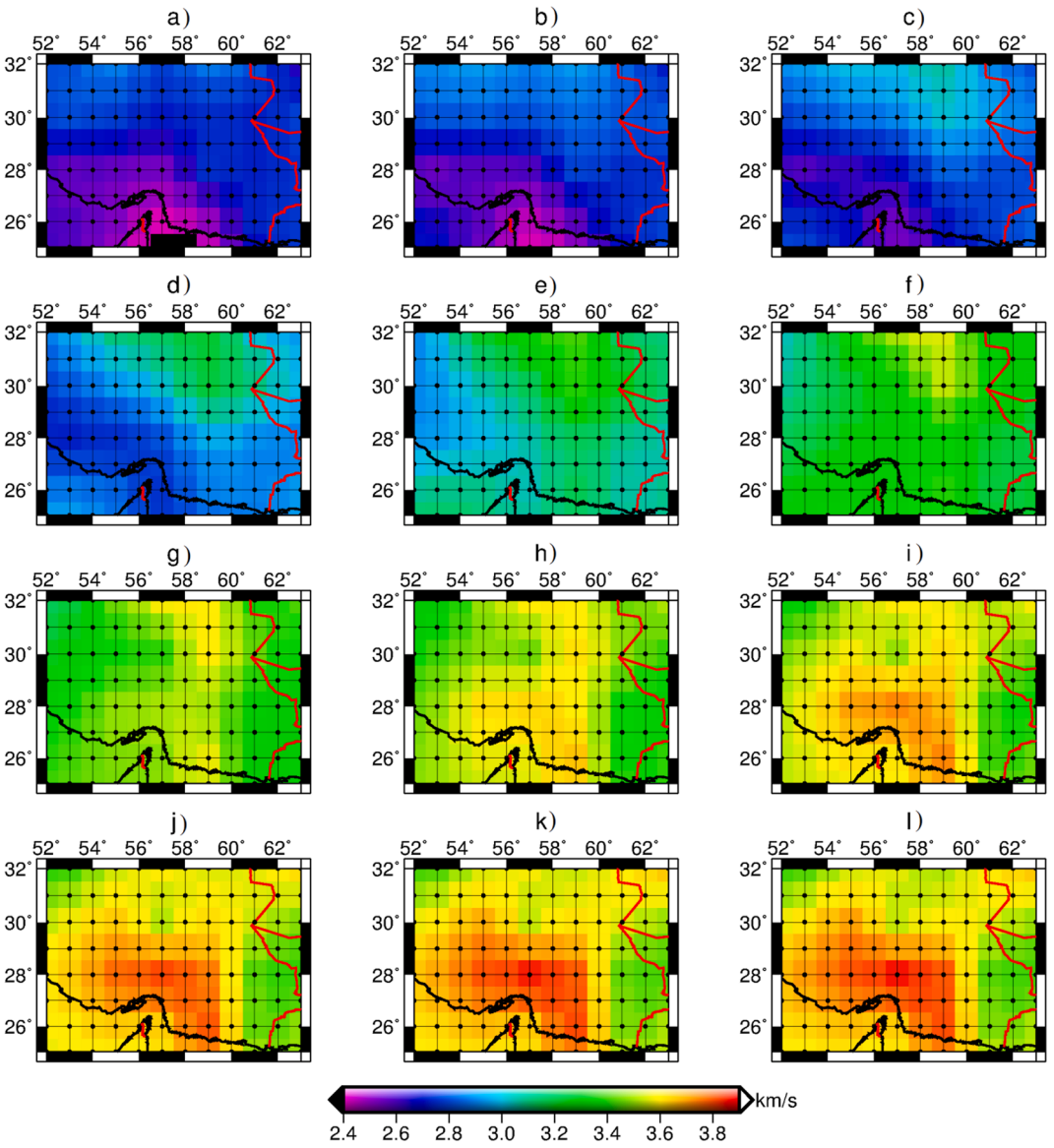

Fig. 2. Rayleigh wave group velocities at periods of (a) 5 s, (b) 10 s, (c) 20 s, (d) 30 s, (e) 40 s, (f) 50 s, (g) 60 s, (h) 70 s, (i) 80 s, (j) 90 s, (k) 100 s, and (1) 110 s in SE Iran (Mohammadi et al., 2020).

Few geophysical studies have been conducted in the Makran subduction zone. Here, we introduce the previous studies that are mostly based on seismic and gravity modeling (Table S1 in the Supplementary Material). Across the western Makran, the Moho map resulting from partitioned waveform inversion indicates that the crustal thickness under the Oman seafloor and Makran fore-arc is about 24–30 km (Shad Manaman et al., 2011). Beneath the Makran highlands, the Moho depth is suddenly increasing towards the north, which indicates the starting location of underthrusting of the Arabian oceanic crust under the Iranian plateau. As it has been shown in Fig. S2 in the Supplementary Material, the Moho deepening continues northwards to reach its maximum value of 48–50 km, where the subducting plate bends below the Taftan-Bazman volcanic arc (Shad Manaman et al., 2011; Abdollahi et al., 2018; Abdollahi et al., 2019). The deepest part of the Moho is found around the Taftan volcano (Fig. 1). Also, Shirzad et al. (2019) studied the crustal structure of the collision-subduction zone in the south of Iran based on seismic tomography, using virtual seismometers and they obtained shear wave velocities consistent with the geological features. In eastern Makran, the crustal thickness is increasing from the fore-arc setting to the volcanic arc, where the maximum Moho depth is about 40 km. The Moho map clearly depicts the western edge of the Makran subduction zone, where the Minab fault marks the boundary between the thick continental crust of the Arabian Plate and the thin oceanic crust of Oman sea (Shad Manaman et al., 2011). Also, Molinari and Morelli (2011) found that the average range of Moho depth increases in the Makran region from S to N from 25 to 45 km. The shear-wave velocity images of the upper mantle across the Makran subduction zone depict a high-velocity anomaly under the Oman seafloor, which is subducting under the entire zone of the Makran belt (Shad Manaman et al., 2011). These authors show that the high-velocity slab of the Arabian plate subducts northward beneath the low-velocity overriding lithosphere of the Lut block in the western Makran and of the Helmand block in the eastern Makran. Taghizadeh-Farahmand et al. (2014), using detailed P-wave receiver functions, estimated an average Moho depth at about 33 ± 2 km beneath the Makran subduction zone. They suggested that this region has a normal continental crust, which has not been influenced by collisional processes.

Kopp et al. (2000) confirmed that the sediment thickness in the Makran subduction zone is extremely high, reaching more than 7 km at the deformation front. Wide-angle seismic lines show an oceanic crustal

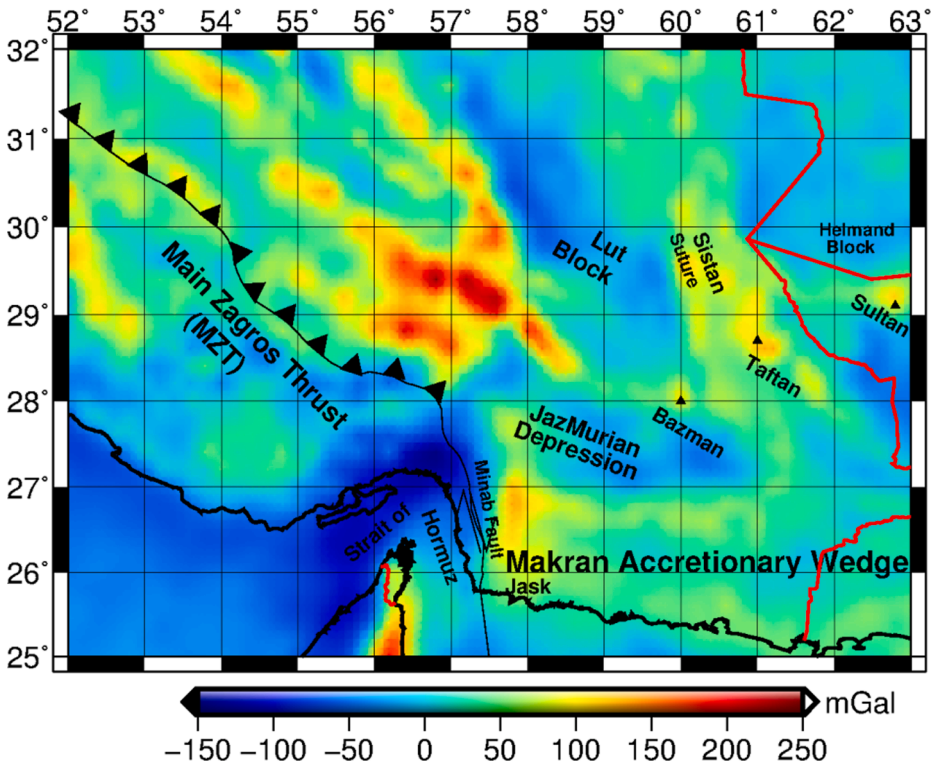

Fig. 3. Free-air gravity anomaly data in SE Iran (http://bgi.omp.obs-mip.fr/).

thickness of about 9 km to the south of the deformation front. The oceanic crust is covered by more than 7 km of undeformed sediments at the front of the wedge. The total thickness of deformed and undeformed sediments reaches more than 10 km near the coastline (Minshull et al., 1992; Kopp et al., 2000).

Low density of seismic stations and events in SE Iran resulted in improper data coverage which in turn made it impossible to conduct high-resolution imaging of density and velocity for this region. Recently, new studies in the Makran subduction zone have been conducted to render the deep structures of the region (Shad Manaman et al., 2011; Molinari and Morelli, 2011; Abdollahi et al., 2018; Abdollahi et al., 2019). In this study, our purpose is to constrain the seismic wave velocity variations and density structure of the sediments, crust and upper-mantle in SE Iran with a new method (using Simulated Annealing (SA) method) and new data as well. Our data are Rayleigh wave group velocity dispersion curves and gravity anomalies. In recent surveys, Rayleigh wave group velocities have been used as a tool to estimate shear and compressional wave velocities and density variation at different depths to characterize the crust and upper mantle structure (Herrmann and Mitchell, 1975; Julia et al., 2000; Kaviani et al., 2007; Rahimi et al., 2014; Motaghi et al., 2015).

Some attempts have been made to use the SA method for real geophysical data, particularly for near-surface seismic data (with a maximum depth of investigation of around 10 m) (e.g. Beaty et al., 2002; Beaty and Schmitt, 2003; Ryden and Park, 2006; Pei et al., 2008; Lu et al., 2016). Furthermore, Iglesias et al. (2001) and Shapiro and Ritzwoller (2002) have used this methods and compared it with the genetic algorithm and Monte Carlo methods for deep structures.

Therefore, we implemented and tested a new inversion procedure for Rayleigh wave group velocity dispersion curves based on this method. The SA algorithm is a global optimization strategy for which we tested the calculation efficiency and stability of the proposed inverse procedure on synthetic models and a real data set in SE Iran. Theoretically, the dispersion curve is a nonlinear function of shear wave velocity, compressional wave velocity and density of the media (Bucher and Smith, 1971). However, it has been proven that surface wave dispersion curves are primarily sensitive to shear wave velocities and the sensitivity for density is much smaller than the one for the velocity (Aki and Richards, 2002; Bucher and Smith, 1971). On the other hand, gravity data may be used to constrain the density distribution. In this way, surface wave dispersion curves, which are good for placing layer limits at depth, and gravity data, which are sensitive to lateral density variations give complementary information and increase the overall resolution of crustal and upper mantle structures. Therefore, we propose here to carry out a sequential inversion of wave dispersion curves and gravity data. We expect to obtain a three-dimensional density model with well-constrained discontinuities in addition to shear (and compressional) wave velocity distribution.

2. Data and methods

2.1. Rayleigh wave group velocity data

Our dispersion velocity data set consists of fundamental-mode Rayleigh wave group velocities at periods of 5 s, 10 s, 20 s, 30 s, 40 s, 50 s, 60 s, 70 s, 80 s, 90 s, 100 s and 110 s for each point on a grid of 1° by 1° in SE Iran between 52 and 63°E and 25-32°N (Fig. 2).

These dispersion observations were taken from a surface wave tomographic study in the Iranian plateau (Mohammadi et al., 2020; Mohammadi, 2020). The data include group velocity dispersion curves extracted from local earthquakes distributed inside Iran and in adjacent areas taking place from 2005 to 2016 with a surface-wave magnitude (Ms) range between 5.0 and 6.5 recorded by the 19 broad-band stations of the International Institute of Earthquake Engineering and Seismology (IIEES).

The checkerboard resolution test results of the observed data and the ray-path coverage for all periods between 5 and 110 s suggest that the resolution is good for most periods in the region and indicates that the pattern and absolute amplitude values were well recovered (Mohammadi, 2020). However, they pointed out that the resolution is rather low for the easternmost and southernmost areas of the region, due to a smaller station density and low path coverage. Hence, the inversion

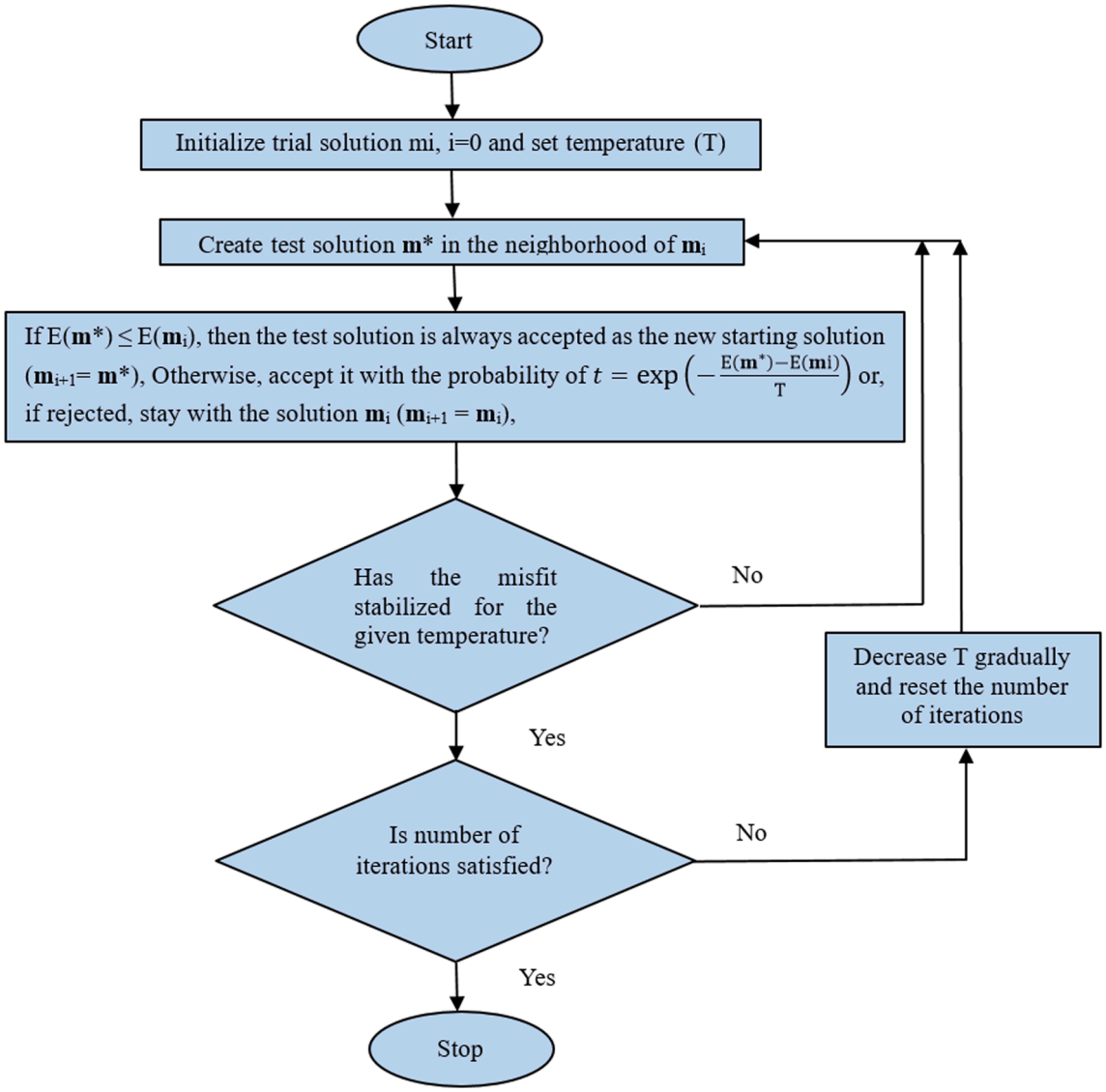

Fig. 4. Simulated Annealing (SA) flowchart.

process does not recover the velocity variations in these areas sufficiently well (Mohammadi, 2020). Ray path distribution images have been shown in Fig. S3, as given by Mohammadi (2020). Some of the checker-board resolution tests at periods of 15, 40, 80, and 110 s, have been shown in Fig. S4. The area with acceptable resolution is marked by a red trapezoid contour in Figs. S3 and S4.

2.2. Gravity data

The gravity data used for inversion come from freely accessible global free-air gravity data with a resolution of 2.5 × 2.5 arc-minutes (https://bgi.omp.obs-mip.fr/), which are extracted and then projected onto a rectangular grid in Cartesian coordinates with 20 km by 22 km (corresponding to 0.2° by 0.2°) grid spacing (Fig. 3).

The free-air gravity anomaly over the Taftan-Bazman and Sultan volcanic arc and the onshore part of the Makran accretionary prism are positive with values above + 100 mGal, reflecting the denser volcanic rocks and the dense subducting slab. The Makran deformation front is marked by a negative anomaly, which stays slightly negative as usual over oceanic crust and becomes strongly positive in the area of the Oman ophiolites.

2.3. Simulated Annealing (SA) method

Typical geophysical inversion problems are ill-posed, nonlinear and non-unique. To deal with the difficulties of non-uniqueness, ill-conditioning and nonlinearity, some stochastic approaches, like the Simulated Annealing (SA) algorithm are proposed. SA is a probabilistic technique for finding the global optimum of a given function. It is especially useful for global optimization in a large search space. The SA method explores initially the whole model space and can thus avoid getting stuck in local minima. In fact, SA is an extension of Markov-Chain Monte Carlo with the same creation method but differing in the acceptance of the new models. Its development was inspired by the physical annealing of metals, where an orderly minimum-energy crystal structure develops within the metal as it is slowly cooling (Černý, 1985; Kirkpatrick et al., 1983).

The SA algorithm starts with a trial solution $\mathbf{m}_0$, randomly chosen within a given model space, where $\mathbf{m}_0$ is a vector containing all elements of a geophysical model (see later). This solution will have a corresponding misfit $E(\mathbf{m}_0)$, which, in our case, is defined as the sum of squared differences between synthetic or measured and calculated Rayleigh wave group velocities (Fig. 4). This misfit is used as the cost function to be minimized.

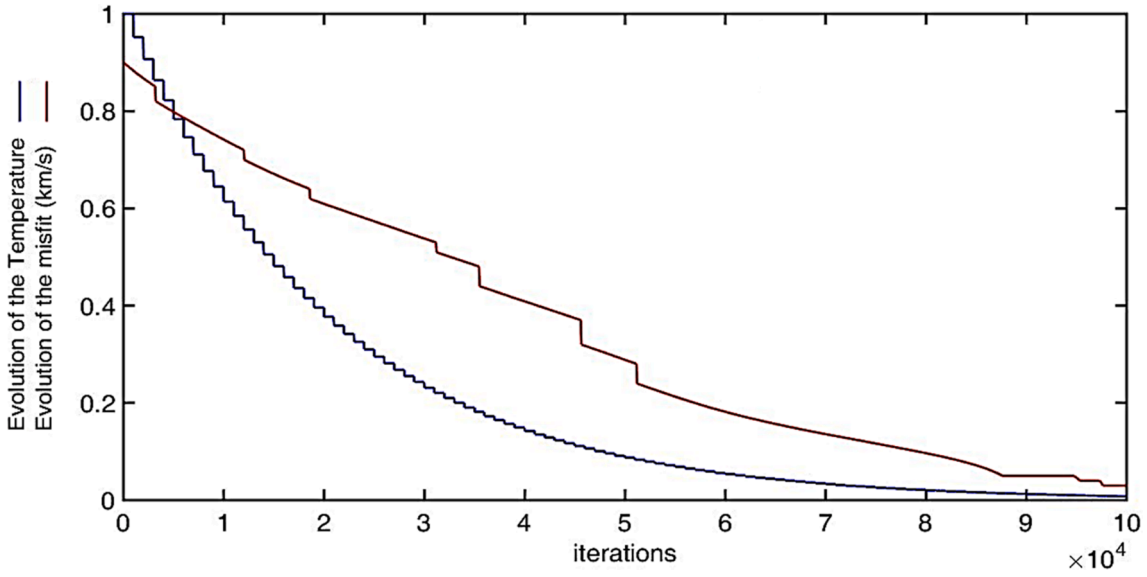

Fig. 5. The evolution of the misfit of the best model and the evolution of T.

A test solution **m*** with the cost function E(**m***) is then generated, located in the neighbourhood of $\mathbf{m_i}$, for example by adding $\mathbf{dm_i}$ to $\mathbf{m_i}$ with a Gaussian distribution for each model parameter $dm_{i,j}$. If $\Delta E = E(\mathbf{m}^*) - E(\mathbf{m_i}) < 0$, the test solution is always accepted as the new trial solution ($\mathbf{m}_{i+1} = \mathbf{m}^*$), but it is also sometimes accepted even if $\Delta E > 0$. In this case, a test parameter, t, based on equation (1) is computed:

$$t = exp\left(-\frac{\Delta E}{T}\right), \tag{1}$$

where T is a normalization factor, corresponding to the metallurgic temperature. Then, a random number "r" that is uniformly distributed on the interval [0,1] is generated and the solution **m*** is accepted if $t > r$.

Large values of T make the algorithm behave as a random, undirected Monte Carlo search since the parameter t is always close to unity and **m*** is nearly always accepted, regardless of the misfit value. Small values lead to reducing the number of accepted models and thus to a reduction of the search space since the parameter t is nearly always close to zero and **m*** is rarely accepted if it has a larger misfit than the previous model. This corresponds to the directed search case, since only such solutions that decrease the error are then accepted (Menke, 2012). As in the physical annealing, the process begins with a large value of T, thus exploring the whole model space. Then T decreases slowly as more and more solutions are examined, restricting the search in the vicinity of the trial model with the smallest misfit. In all presented inversions, we started with a value of 1 for T and reduced it every 1000 iteration by a factor of 0.95 (Fig. 5).

Simulated Annealing has proven to be quite useful for determining velocity parameters from dispersion curve data but is computationally quite expensive. However, this method is much faster than the Markov-Chain Monte Carlo (MCMC) method since it reduces the number of trial models and reduces thus the calculation time, the main drawback of the MCMC method. A drawback is that SA is only able to give approximate information on the uncertainty of the resulting values. It is, however, capable of finding the best final model.

2.4. Surface wave velocity analysis

Generally, dispersion curves are inverted in 1D using a large number of thin layers considering a constant velocity in each layer (e.g. Mitchell and Herrmann, 1979; Yamanaka and Ishida, 1996; Herrmann and Ammon, 2007; Beaty and Schmitt, 2003; Herrmann, 2013).

The method by Herrmann (2013) is well established but has the inconvenience that it may be difficult to locate geological layer limits such as the base of a sedimentary basin or the crust-mantle boundary (Moho) based on the inversion results due to often relatively smooth transitions in the resulting models. We chose therefore to use another approach. The area of interest is subdivided into rectangular columns of constant size in E–W (X) and N–S (Y) direction, one column per available dispersion curve point. In depth (Z), each column is subdivided into four layers: sediments, upper and lower crust, and lithospheric mantle. In each layer and each column, we consider velocities and densities to have a linear vertical gradient. We are thus looking for the layer thickness, average P-wave (compressional, α) and S-wave velocity (shear, β) the average density ρ, as well as the vertical gradients of the three physical properties. So, with 7 parameters in the four main layers, we have 28 parameters at each data point. After several sensitivity tests, we fixed the base of the model at 200 km reducing the number of unknowns to 27 per data point. We then investigated the sensitivity of the group velocities on variations of each parameter, varying one at a time over a range of ± 5%. In this way, we obtained partial derivatives:

$$\left\{\frac{\partial U_{T_i}}{\partial \alpha_n}, \frac{\partial U_{T_i}}{\partial \nabla \alpha_n}, \frac{\partial U_{T_i}}{\partial \beta_n}, \frac{\partial U_{T_i}}{\partial \nabla \beta_n}, \frac{\partial U_{T_i}}{\partial \rho_n}, \frac{\partial U_{T_i}}{\partial \nabla \rho_n}, \frac{\partial U_{T_i}}{\partial h_n}\right\}, i = 1:12, n = 1:4, \tag{2}$$

where h_n is the layer thickness, T_i is period, i is the period number and n is the layer number. As reference, we used the global crustal model, CRUST 1.0 (Laske and Masters, 2013) for these calculations.

For this model, the Rayleigh surface wave group velocities were calculated at the above-mentioned 12 periods $\boldsymbol{U}_0 = (u_{T1}, u_{T2}, u_{T3}, u_{T4}, u_{T5}, u_{T6}, u_{T7}, u_{T8}, u_{T9}, u_{T10}, u_{T11}, u_{T12})$ using Herrmann's SURF96 program suite (Herrmann, 2013). We observed that the sensitivity of the sediment layer to the change in velocity and density gradients is low and even zero for sediment thicknesses below 6 km (Figs. S5 and S6 in the Supplementary Material). Thus, their effect can be neglected, and it is enough to use only the average values of velocity and density for sediments, reducing the number of unknowns per data point to 24. Also, we replaced the compressional velocity by the ratio of compressional to shear wave velocity (Vp/Vs) which we considered constant within each layer, eliminating in this way three more unknowns, the vertical gradients of the compressional wave velocity. In the end, we fixed the density at the lithosphere-asthenosphere boundary (LAB) to 3200 kg/m^3 (e.g. Lachenbruch and Morgan, 1990), by which the total number of unknowns per data point reduces to 20.

To calculate the group velocities correctly in the presence of a vertical velocity gradient, the different layers (upper crust, lower-crust, and

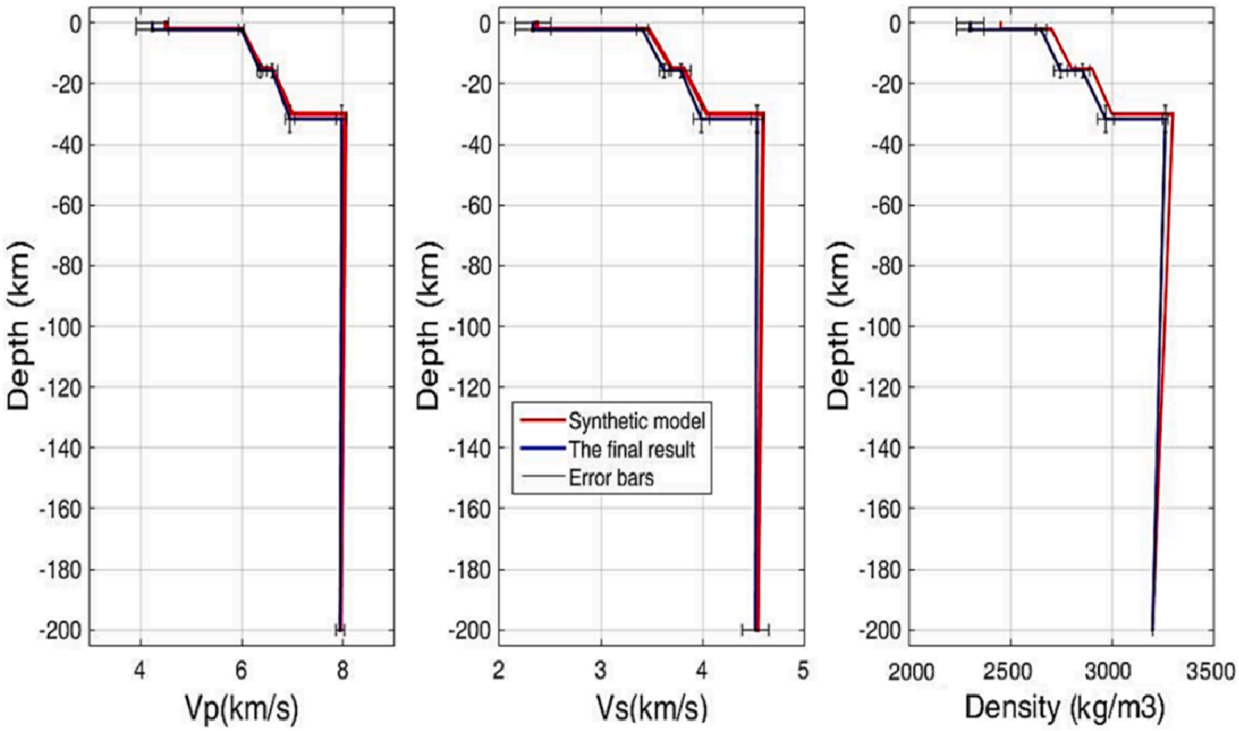

Fig. 6. Inversion results of a noise-free synthetic model (red line) and the best model resulting from the SA inversion method (blue line) with 1 sigma uncertainties (black error bars).

uppermost mantle) have to be subdivided into a number of sub-layers with constant parameter values. To estimate the most appropriate thickness for those sub-layers we repeated the calculations for different numbers of sub-layers. For each layer, the result for U was calculated by subdividing the layer into sub-layers with decreasing thickness. For thick sub-layers, the result depends on the number of layers, whereas for thin layers from a certain maximum thickness, the result stays stable. In this way, we determined the following maximum thickness of the sub-layers for each geological layer: 3 km for the upper crustal sub-layers, 4 km for those of the lower-crust, and 11 km for the mantle sub-layers. Since no vertical gradient is applied in the sediments, this layer does not have to be subdivided. The misfit to be minimized durimg the SA inversion is thus defined as:

$$E = \sum_{i=Periods} (U_{i\_measured} - U_{i\_calculated})^2, \mathrm{i} = 1:12 \tag{3}$$

where U are the Rayleigh wave velocities for the 12 periods obtained at every data point.

2.5. Gravity modeling

As mentioned above, the dispersion curve is a nonlinear function of shear and compressional wave velocity and density of the media. However, the sensitivity to shear wave velocity is much higher than the sensitivity to density. So, we have done gravity modeling to increase the resolution of the density model. The gravitational effect of a rectangular column with a linear vertical density variation can be calculated using the analytical formula of Gallardo-Delgado et al. (2003):

$$\Delta g = G\rho_0 \left[\left[\left[x*\ln(y+r) + y*\ln(x+r) - z*\arctan\left(\frac{xy}{zr}\right)\right]_{x_1}^{x_2}\right]_{y_1}^{y_2}\right]_{z_1}^{z_2}$$

$$+ G\gamma \left[\left[\left[-xy*\ln(r+z) - \frac{z^2}{2}\arctan\left(\frac{xy}{zr}\right) + \frac{x^2}{2}\arctan\left(\frac{yz}{yr}\right) + \frac{y^2}{2}\arctan\left(\frac{xz}{yr}\right)\right]_{x_1}^{x_2}\right]_{y_1}^{y_2}\right]_{z_1}^{z_2}$$

$$r = \sqrt{x^2+y^2+z^2}, \quad \rho(z) = \rho_0 + \gamma z, \tag{4}$$

where G is the gravitational constant ($6.6726 \times 10^{-11} m^3 s^{-2} kg^{-1}$), ($x_1$, x_2) is the distance between a measurement point and the two vertical N-S faces of the column, (y_1,y_2) is the distance between a measurement point and the two vertical E-W faces of the column and (z_1,z_2) is the distance between a measurement point and the upper and lower boundary of the column. The brackets represent summation over the integral limits (positive for the upper bound, negative for the lower bound). Summation over all columns gives the 3D gravitational effect of the model. The model parameters that are to be found in the gravity inversion procedure are the thickness, and the average density of sediments, upper-crust, lower-crust and upper-mantle in each column under the constraint to keep depths as near as possible to the surface wave model.

The area of interest is also here subdivided into rectangular columns of constant size 1° by 1° in E–W (X: 52°-63°) and N–S (Y: 25°–32°) direction. In depth (Z), each column is subdivided into four layers: sediment, upper crust, lower crust and upper mantle. The distance between the gravity data points is 0.2° by 0.2°. The data vector is thus:

$$d^T = [d_1, \cdots, d_{Ng}] = [\Delta g_1, \cdots, \Delta g_{Ng}], \tag{5}$$

where Ng is the total number of gravity data points. The inverse problem involves minimizing the following cost function (Zeyen and Pous, 1993):

$$CF = \epsilon_d + \lambda\epsilon_p = \Delta \boldsymbol{d}^T C_d^{-1} \Delta \boldsymbol{d} + \lambda(\boldsymbol{p} - \boldsymbol{p}_0)^T C_p^{-1}(\boldsymbol{p} - \boldsymbol{p}_0). \tag{6}$$

Here, $\Delta\mathbf{d}$ is the vector of differences between the measured data and

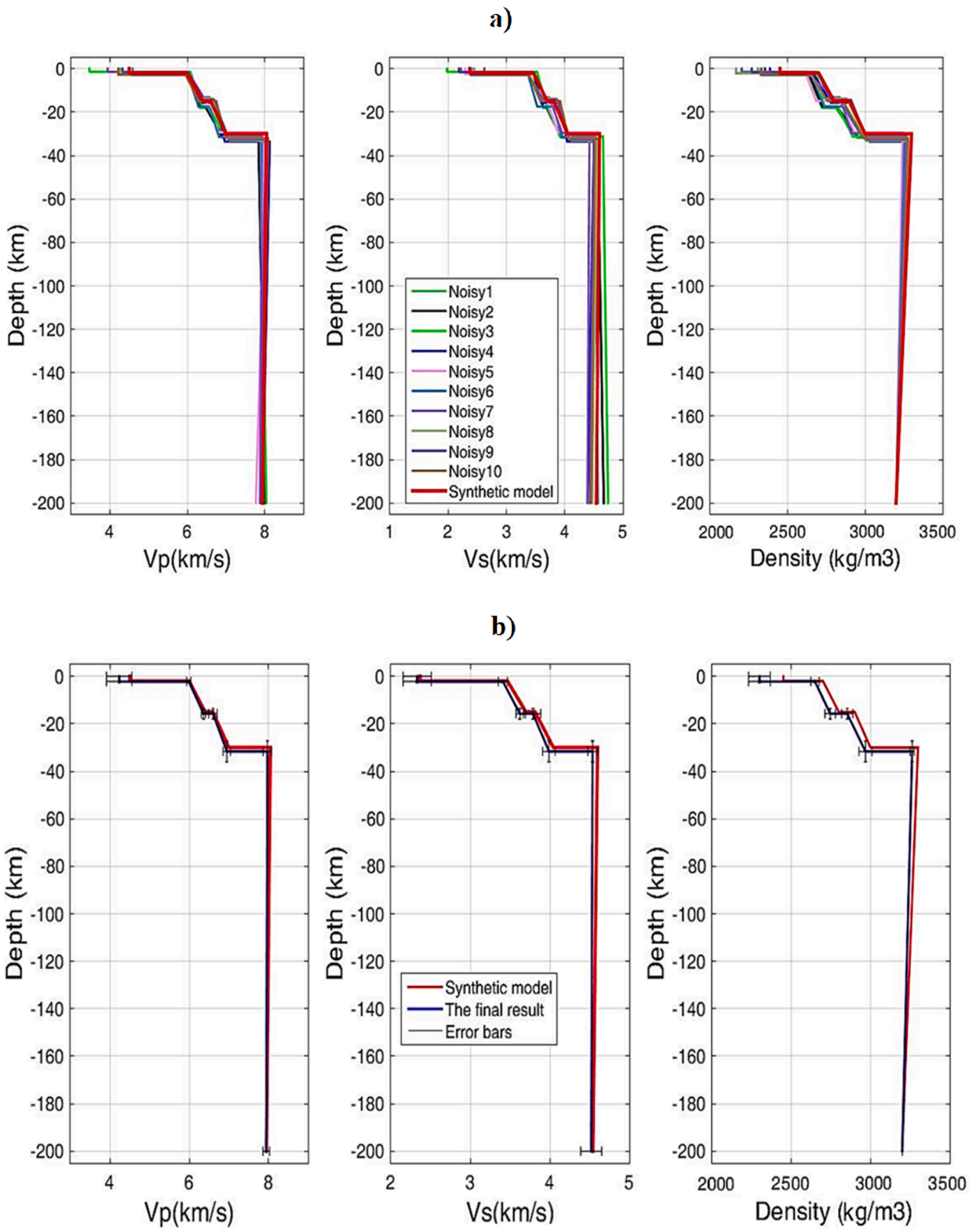

Fig. 7. Inversion results of a synthetic model based on SA method. (a) with 10 different random Gaussian noise realizations. All 10 data sets (with different random noise) have been inverted 15 times separately and all 10 best models with minimum misfit have been plotted with different colors, (b) synthetic model (red line) and the average of the aforementioned 10 best results as the final result (blue line) with 1 sigma uncertainties (black error bars).

those calculated with model parameters **p** (densities of all blocks) and $\mathbf{C}_d$ is the variance matrix of the data, containing on the diagonal the squared uncertainty of each data point. Vector **p** contains the model parameters, $\mathbf{p_0}$ is the vector of initial parameters coming from the surface wave inversion and $\mathbf{C}_p$ the variance matrix of the parameters which has on its diagonal the uncertainties (variability) σ_p^2 of the parameters. The program minimizes two terms, the relative importance of which may be controlled by the user through the parameter λ. The first

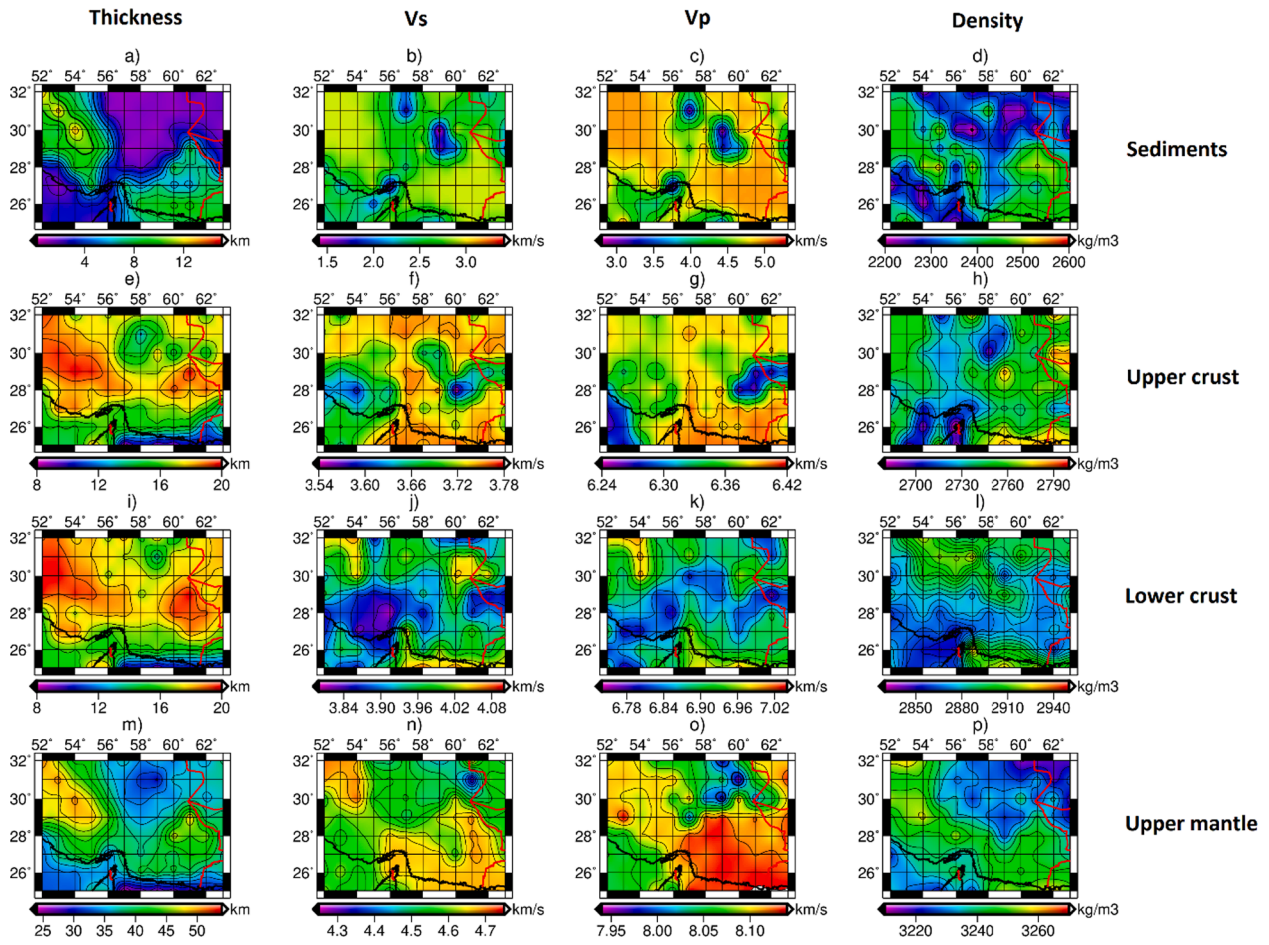

Fig. 8. The final model based on the SA inversion. (a) Thickness of sediments (km), (b) Vs in the sediment layer (km/s), (c) Vp in the sediment layer (km/s), (d) density of the sediments (kg/m^3), (e) thickness of upper crust (km), (f) average Vs of upper crust (km/s), (g) average Vp of upper crust (km/s), (h) average density of upper crust (kg/m^3), (i) thickness of lower crust (km), (j) average Vs of lower crust (km/s), (k) average Vp of lower crust (km/s), (l) average density of lower crust (kg/m^3), (m) Moho depth (km), (n) average Vs of mantle lithosphere (km/s), (o) average Vp of mantle lithosphere (km/s), and(p) average density of mantle lithosphere (kg/m^3).

term corresponds to the data misfit and the second term to the distance of the final model from the initial model containing, if available, a priori information. If λ is small, data adjustment controls the inversion process and parameters may change more freely, which may introduce stability problems if the initial parameter set is too far away from the optimum set. On the other hand, if λ is large, the parameters are forced to stay near their initial values at the expense of a good data fit. In principle, λ should be used as small as possible so that the inversion remains stable without smoothing the solution too much.

In our algorithm, p_0 is updated in every iteration step with the values obtained from the last iteration. In this way, the parameters are not necessarily forced to stay near the initial values, except for those having a small σ_p i.e. where prior knowledge is available as for the depths of interfaces coming from the Rayleigh wave inversion (Zeyen et al., 2005; Zeyen and Pous, 1993).

Minimizing the cost function (5) ultimately takes the following iterative form (Menke, 2012):

$$p^{k+1} = p^k + \left(G^T C_d^{-1} G + \lambda C_p^{-1}\right)^{-1} \left(G^T C_d^{-1} \Delta d\right), \tag{7}$$

here k is the number of iterations and G is the Fréchet derivative matrix. Typically a few tens of iterations are necessary to obtain a stable result.

3. Results

3.1. Synthetic data inversion based on the SA method

In order to show the utility of the SA inversion method for 1D Rayleigh wave dispersion curves, we applied this method to an arbitrary noise-free and its corresponding noisy synthetic 1D model that is shown in the Supplementary Material, Table S2. We defined a search space range based on global crustal models for densities and velocities (e.g. Laske and Masters, 2013) and selected the parameters of the synthetic model partly near the center of the defined search space and partly near the boundaries of the search space to test the ability of our method to detect also unexpected, abnormal parameter values.

For noise-free synthetic data, the number of iterations was selected as 100,000 and the inversion was repeated 10 times (Table S2 in the Supplementary Material). Fig. 6 shows the noise-free synthetic model and its final result. However, real surface wave velocities are always noisy. The addition of noise often introduces complications and, therefore, the robustness of an inversion algorithm can be judged only after applying it to the noisy data. Mohammadi (2020) report maximum uncertainties of Rayleigh wave group velocities of ± 0.1 km/s. Therefore, we perturbed the synthetic Rayleigh wave group velocities of the synthetic model by adding white Gaussian noise with a sigma of 0.1 km/s. For the noisy data, we constructed 10 different data sets by adding 10 different realizations of random noise to the data, considering that the inversion result of a single noisy data set is not necessarily comparable

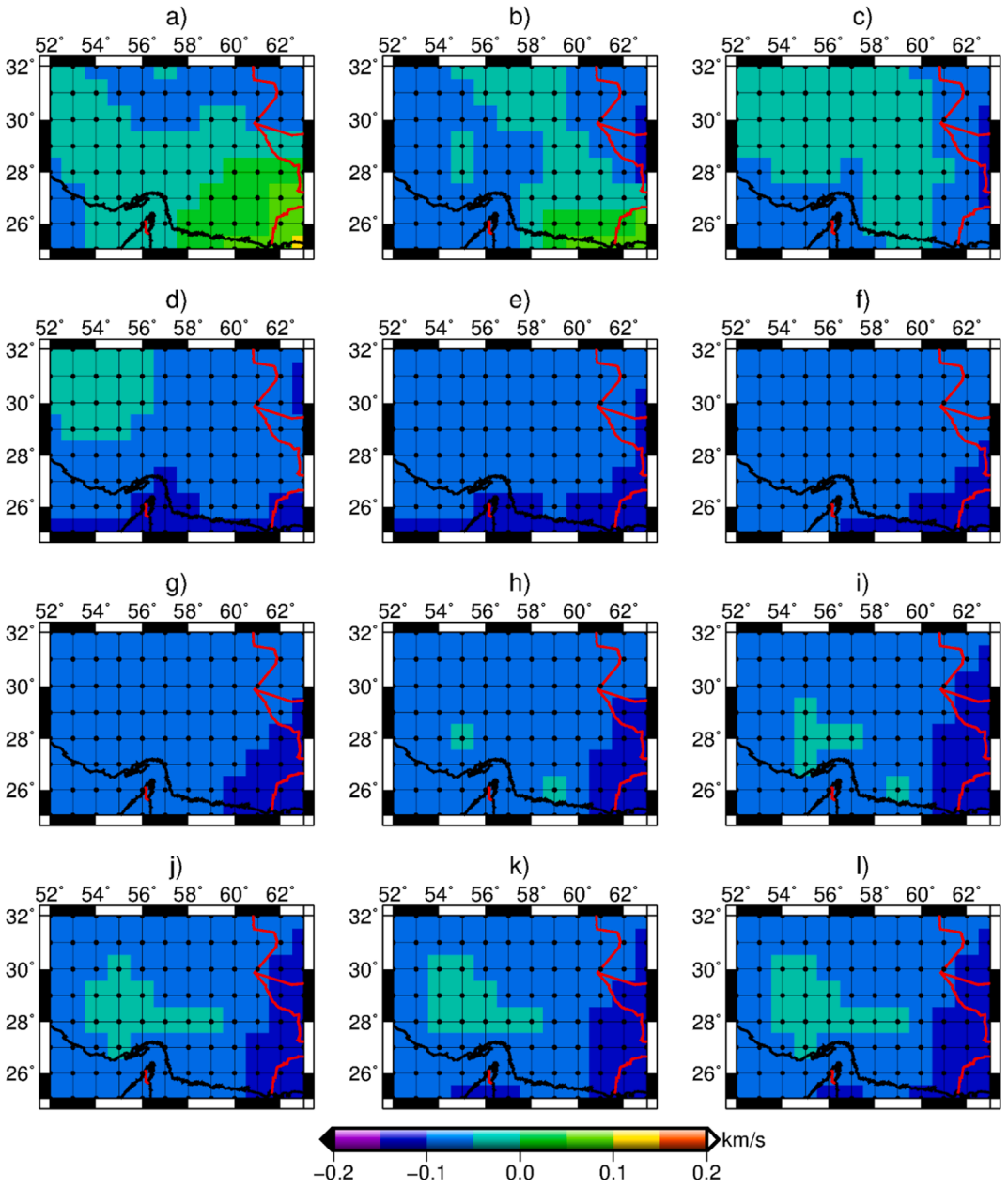

Fig. 9. Data misfit after the first round SA modeling for real data inversion (calculated data minus observed data) for Rayleigh wave group velocity in SE Iran at periods of (a) 5 s, (b) 10 s, (c) 20 s, (d) 30 s, (e) 40 s, (f) 50 s, (g) 60 s, (h) 70 s, (i) 80 s, (j) 90 s, (k) 100 s, and (1) 110 s in SE Iran.

with the synthetic mode, whereas an average of the 10 different models should be near to the synthetic model. Every data set (with different random noise) has been inverted 15 times separately. The average of these 15 best models gave us the final best models for each data set (Tables S3 and S4 in the Supplementary Material and Fig. 7a). Fig. 5 shows an example of misfit evolution for the first noisy model.

Thus, the final model was taken as the average of these 10 models and the uncertainty was calculated as the standard deviation of the average of these 10 best models models (Fig. 7b). Relative errors between the true models and parameters estimated from the SA inversions on the noise-free and noisy data sets are displayed in the Supplementary Material, Tables S2, S3 and S4.

3.2. Real data inversion based on the SA method

Since the results from the synthetic data demonstrate that the SA method can be successfully applied to the nonlinear inversion of surface wave data, we used this method to invert the Rayleigh wave dispersion curve data of SE Iran. Our area is subdivided into a rectangular grid, with columns having a constant size of 1° by 1° in E-W (X: 52°-63°) and N-S (Y: 25°–32°). So, the total number of grid points is $N_{xy} = (N_x{*}N_y) = (12{*}8) = 96$. In the vertical direction (Z), each column is divided into four layers: sediments, upper crust, lower crust, and lithospheric mantle with 20 unknowns (N_M), as mentioned above. Hence, the total number of unknowns is $N_m = N_{xy}{*}N_M = 96{*}20 = 1920$. However, these 1920 unknowns were not inverted altogether in a SA single run. In fact, each column with 20 unknowns has been inverted independently and the total number of columns (grid points) is 96, then 96 independent inversions have been done.

Our dispersion velocity data set consists of fundamental-mode Rayleigh wave group velocities at periods of 5 s, 10 s, 20 s, 30 s, 40 s, 50 s, 60 s, 70 s, 80 s, 90 s, 100 s, and 110 s for each point on a grid of 1° by 1° in SE Iran between 52 and 63E and 25–32 N. Therefore, the number of group velocity dispersion values for each point on the grid in SE Iran, is

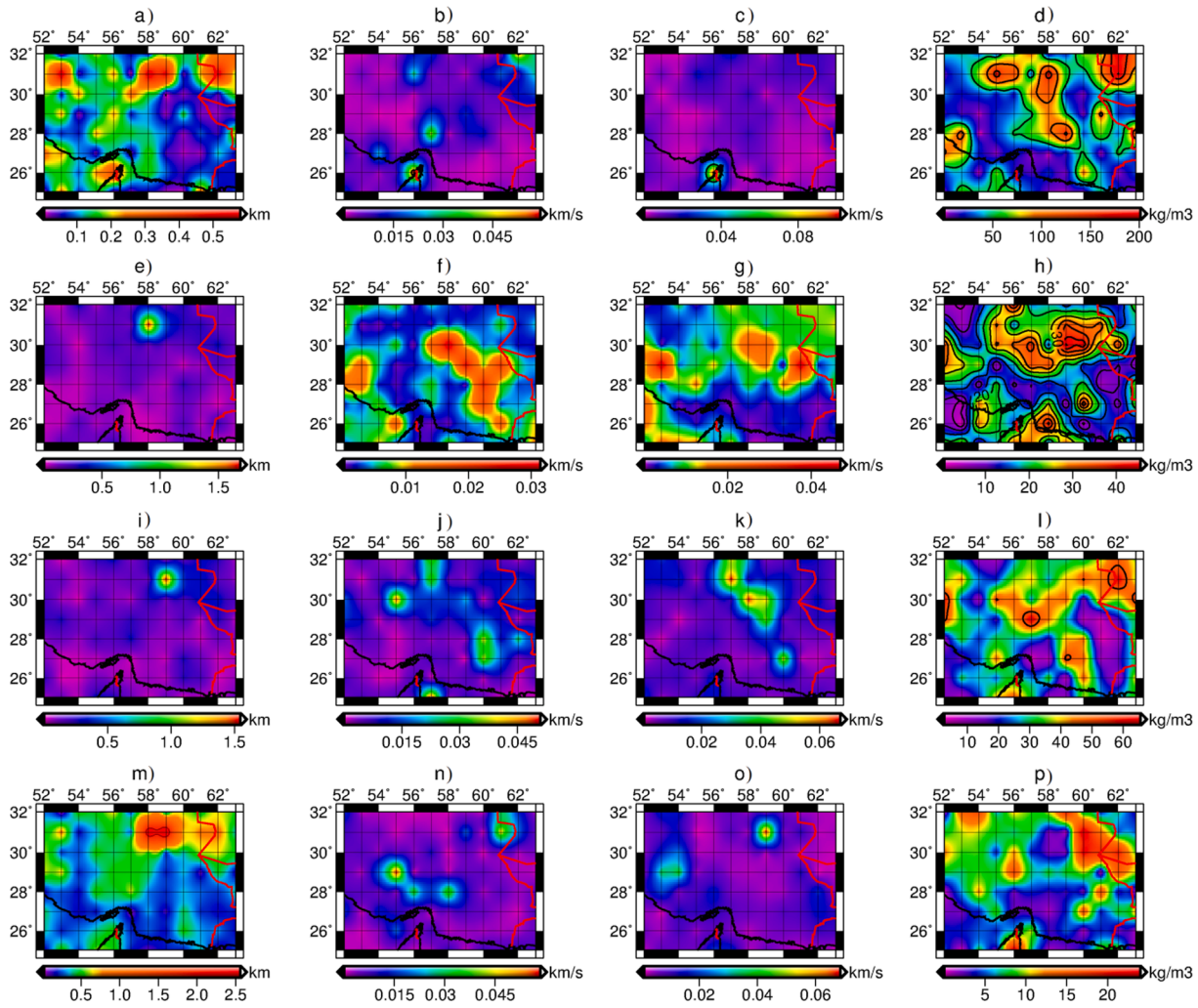

Fig. 10. Maps of uncertainty distribution of the model parameters after the first round of SA modeling: (a) Thickness of sediments (km), (b) Vs of the sediment layer (km/s), (c) Vp of the sediment layer (km/s), (d) density of the sediments (kg/m^3), (e) thickness of upper crust (km), (f) Vs of upper crust (km/s), (g) Vp of upper crust (km/s), (h) density of upper crust (kg/m^3), (i) thickness of lower crust(km), (j) Vs of lower crust (km/s), (k) Vp of lower crust (km/s), (l) density of lower crust (kg/m^3), (m) Moho depth (km), (n) Vs of mantle lithosphere (km/s), (o) Vp of mantle lithosphere (km/s), and (p) density of mantle lithosphere (kg/m^3).

12 and the total number for the all points are $N_u = N_{xy}{}^*N_U = 96{}^*12 = 1152$.

Similar to the inverse strategy for the synthetic data, we applied the SA method to the real data 10 times. The number of performed iterations for each time was 100,000 for every data point with 20 unknowns in which the best model with minimum misfit has been selected for every point and finally, the average of the 10 results was calculated as the final result.

Fig. 8 shows the results for each point in a grid map for all model parameters in the mentioned area. The data misfit for the best fitting model is illustrated in Fig. 9. From the 10 inversion runs with different random starting models and thus different realizations of the random distributions, the standard deviation for each parameter has been calculated and is presented in Fig. 10 as an estimate of the model uncertainty.

3.3. Gravity modeling results

Using the above-mentioned approach on gravity modeling, the density variation and thickness distribution of the different lithosphere layers were obtained, as shown in Fig. 11. The density of the asthenosphere is fixed (3200 kg/m^3) and its base is defined at a constant depth of 200 km as for the surface-wave model.

For the inversion, 5 mGal have been used for the gravity data uncertainty. For the inversion with prior information, thickness uncertainties are reduced to 500 m for the crust and upper mantle thicknesses and 100 m for sediment thickness. Also, 50 kg/m^3 for the density uncertainty have been considered. Furthermore, the coefficient λ was set to 1. After 28 iterations, the inversion stabilized.

3.4. Real data inversion based on the SA method constrained by the results of gravity modeling

In a final step, we used the results of gravity modeling to constrain densities more than other model parameters by performing a second round of surface wave dispersion inversion with the SA algorithm. Therefore, the search space ranges (the same as those given for the synthetic data in Table 2 of the supplementary data) have been reduced by 60% for the densities and by 10% for the thicknesses and velocities and, also, fewer iterations per data point were used (maximum 50,000 iterations). On average, the inversion at a single column takes about 1 min for 500 iterations. The efficiency of the SA techniques depends significantly on the time required for the computations. Therefore, with this approach, the solution space is significantly smaller, resulting in decreased computational time as well.

Results are shown for all parameters in Fig. 12 and data misfits of the

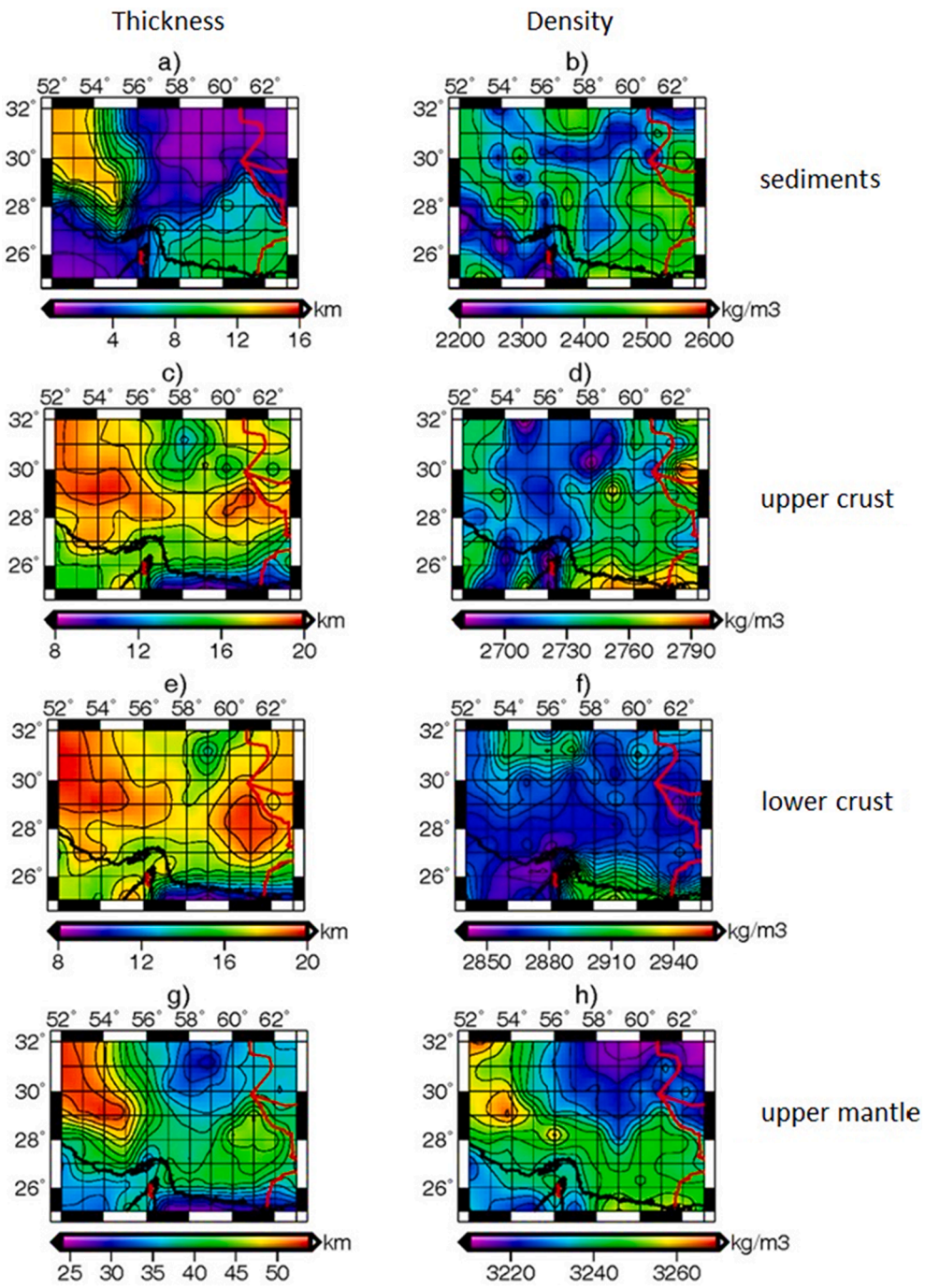

Fig. 11. The final thickness and density model obtained from gravity inversion. (a) Thickness of sediments (km), (b) average density of the sediments (kg/m^3), (c) thickness of upper crust (km), (d) average density of upper crust (kg/m^3), (e) thickness of lower crust (km), (f) average density of lower crust (kg/m^3), (g) Moho depth (km), and (h) average density of mantle lithosphere (kg/m^3).

results are shown in Fig. 13. The new maps of uncertainty distribution in the model parameters are shown in Fig. 14. Finally, the Moho geometry, average crustal shear wave velocity and average crustal density for the region are shown in Fig. 15. The borders of the areas with acceptable resolution has been marked by a red contour.

4. Discussion

In this research, we implemented a sequential inversion of Rayleigh wave group velocity data and gravity anomaly. We used 1D Simulated Annealing inversion of thicknesses of sediments, upper and lower crust, as well as average P and S-wave velocities and densities for these three layers and the lithospheric mantle for the Rayleigh-wave inversion, followed by 3D matrix inversion of gravity data for layer thicknesses and density distribution in these layers constrained by the thicknesses resulting from the SA inversion. In the last step, we redid an SA inversion of the Rayleigh wave data, constraining the model space for thicknesses and especially densities with the results of the gravity inversion. With this method, we established a model of the crust and upper mantle structure of the Makran region in SE Iran.

As shown in Fig. 6, the inversion of noise-free synthetic data resulted in a model very near to the synthetic model even for parameters located near the borders of the parameter space. For the noisy synthetic data, it is clear that one single example of noisy data will not necessarily result

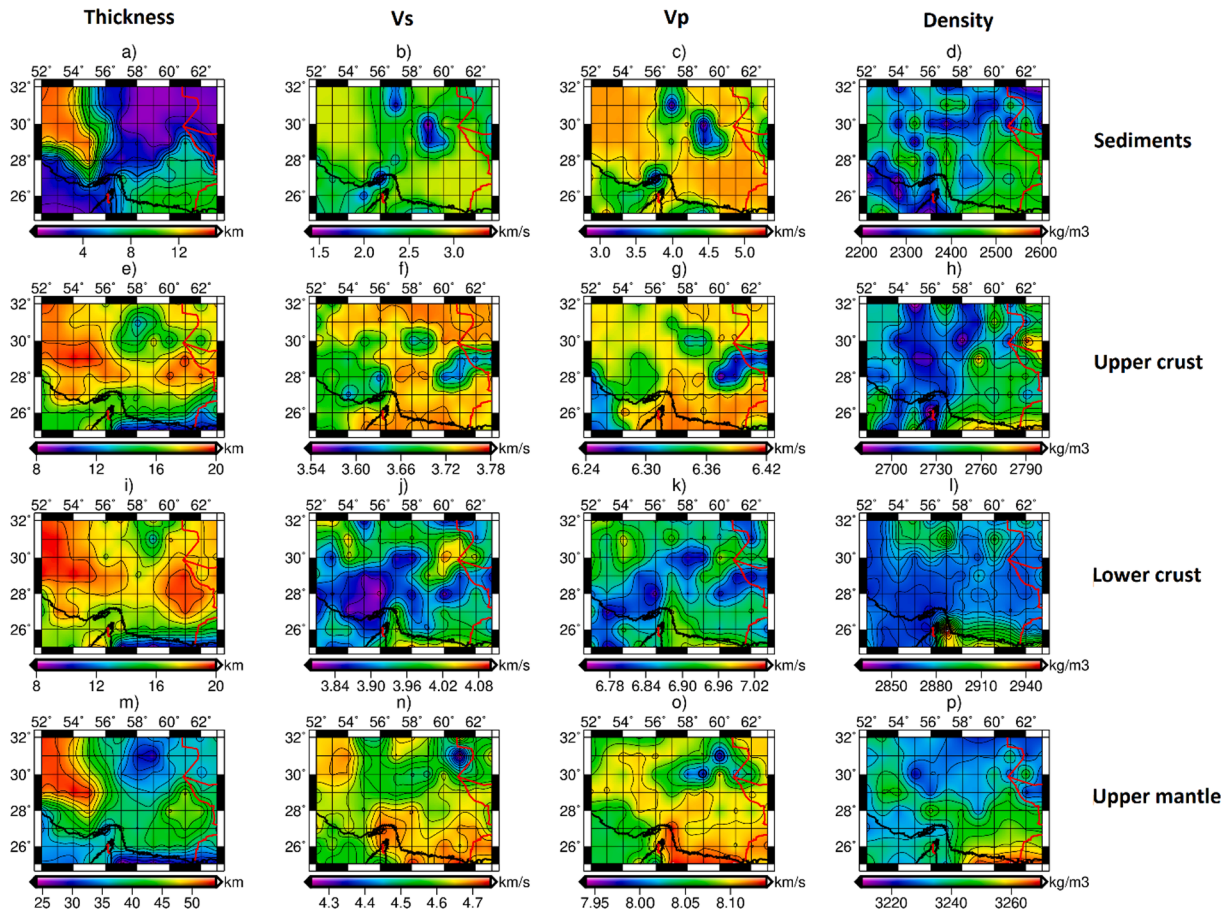

Fig. 12. The final model based on the SA inversion. (a) Thickness of sediments (km), (b) Vs in the sediment layer (km/s), (c) Vp in the sediment layer (km/s), (d) density of the sediments (kg/m3), (e) thickness of upper crust (km), (f) average Vs of upper crust (km/s), (g) average Vp of upper crust (km/s), (h) average density of upper crust (kg/m3), (i) thickness of lower crust(km), (j) average Vs of lower crust (km/s), (k) average Vp of lower crust (km/s), (l) average density of lower crust (kg/m3), (m) Moho depth (km), (n) average Vs of mantle lithosphere (km/s), (o) average Vp of mantle lithosphere (km/s), and (p) average density of mantle lithosphere (kg/m3).

in an optimum model close to the real model. In fact, this is not a problem of the method but of the noisy data. To be able to judge the ability of the procedure to recover the models, we added 10 different versions of random noise to the data and created 10 different data sets, and did the inversion for every data set 15 times separately, resulting in 150 models. As should be expected for a working inversion algorithm, the average of these models resulted close to the synthetic model, showing that the algorithm works well also with noisy data. Evidently, this procedure is only applicable to synthetic data; however, it shows that the algorithm gives the expected results also with noisy data. Relative errors of SA inversion on the noise-free data set were less than 2% for most parameters (see Supplementary Material, Table S2). Also, for the noisy data sets, relative errors stay mostly below 3% except for the sediments which are less well-resolved with the available surface wave periods (Supplementary Material, Tables S3, and S4). Since there is a trade-off between the thickness of the upper and lower crust, we have added a row in the Supplementary Material, Tables S2, S3, and S4. with values for total crustal thickness (Moho depth), since this is, in general, the most interesting result. As we can see in the Supplementary Material, Tables S2, S3, and S4, the results for Moho depth are also close to the synthetic depths.

In a previous study (Abdollahi et al., 2018), we implemented the Shuffled Complex Evolution (SCE) method and it was observed that for the SA method, the variations of the parameter values in successive tests are small in comparison to the SCE method. This indicates that while both methods produce similar efficiency values for final average parameter estimation, the SA is more likely to produce the sets of parameter values that differ least from test to test (Fig. 7a and Tables S3 and S4 in the Supplementary Material). Whereas the SA method is computationally less efficient than the SCE method with respect to the total number of iterations and computing time, considering the smaller variability of the resulting parameter values in successive, independent tests, the SA method can be considered more stable and therefore well suitable for the inversion of surface wave data. Furthermore, it should be pointed out that our new surface wave data have more precision and accuracy (Goswami and O'Connor, 2007).

For real data we used three steps: in the first step, similar to the inverse strategy of the synthetic data, we applied the SA method to the real data 10 times separately. Fig. 8 shows the results and the data misfit for the best fitting model is illustrated in Fig. 9. In most areas, these misfits stay within the +/-0.1 km/s uncertainty estimated by Mohammadi (2020). The maps of uncertainty distribution in the model parameters, calculated as the standard deviation of the results of all 10 inversion runs, are shown in Fig. 10. The uncertainty for layer thicknesses is about 0.05–1.7 km and the Moho uncertainty varies between 0.1 and 2.6 km. Shear velocity uncertainty in sediment, crust and upper mantle is about 0.01–0.06 km/s. The uncertainty for compressional velocity is about 0.01–0.1 km/s. The uncertainty for sediment density is about 10–200 kg/m^3 and for the crust and upper mantle density, it is about 1–65 kg/m^3 (Fig. 10). The uncertainties for densities, especially in the sediments, are thus considerable.

In a second step, we have done 3D gravity modeling to increase the resolution of the density model, constraining the depths of the layer interfaces by the result of the Rayleigh wave inversion. Comparison of

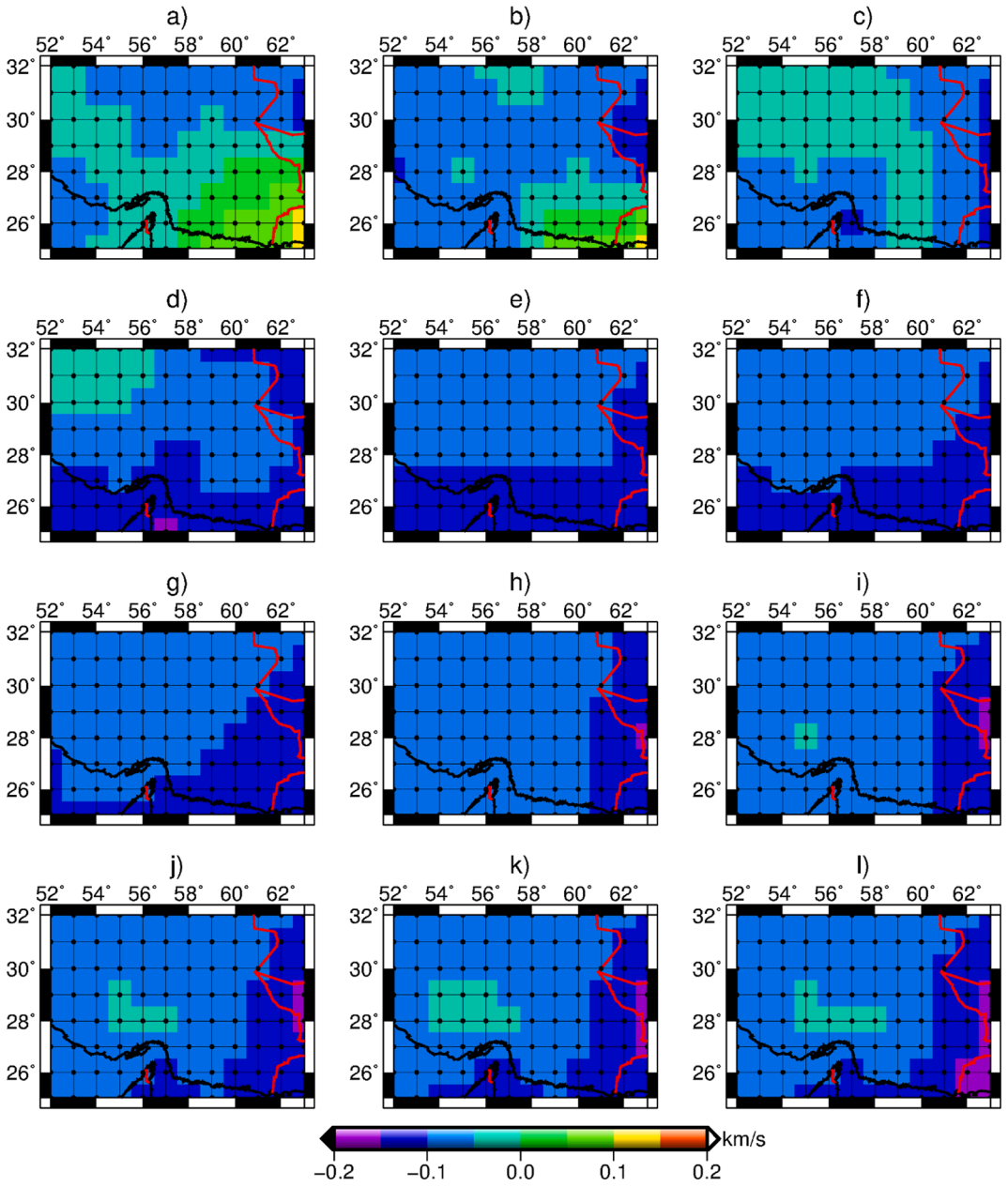

Fig. 13. Data misfit after the second round SA modeling for real data inversion (calculated data minus observed data) for Rayleigh wave group velocity in SE Iran at periods of (a) 5 s, (b) 10 s, (c) 20 s, (d) 30 s, (e) 40 s, (f) 50 s, (g) 60 s, (h) 70 s, (i) 80 s, (j) 90 s, (k) 100 s, and (l) 110 s in SE Iran.

Figs. 8 and 11 shows that the thicknesses and densities have been changed slightly and in some points are somewhat different, which is acceptable.

In a final step, the resulting model from gravity inversion was used as the starting model and to constrain densities, reducing the search space in the second run of SA inversion of group velocities. Similar to the first round of SA modeling, we applied the SA method to the real data 10 times again. Therefore, the best model with minimum misfit has been selected for every point and finally, the average of the 10 results was calculated as the final best result. The resulting uncertainties were thus reduced and result for layer thicknesses is about 0.05–0.6 km and the Moho uncertainty varies between 0.1 and 1.6 km. Shear velocity uncertainty in sediment, crust and upper mantle is about 0.005–0.05 km/s. The uncertainty for compressional velocity is about 0.005–0.06 and the uncertainty for sediment density is also about 1–24 kg/m^3 and for the crust and upper mantle, density is also about 1–16 kg/m^3 (Fig. 14). As it is obvious from this analysis, the uncertainties for densities, especially sediment density have been reduced considerably, as could be expected. The uncertainties for velocities and thickness have been reduced slightly.

The average velocity data misfits for all mentioned 12 periods increased slightly from values between 0.05 and 0.08 km/s after the first SA run to 0.06 to 0.1 km/s after the second SA run (compare Figs. 9 and 13). Hence, as may be expected, the data misfit of the final model increases when adding constraints on the model parameters in comparison with the unconstrained inversion. However, this increase is not significant and stays nearly everywhere within the estimated data uncertainties. This is mainly an effect of the gravity constraint, which imposes some lateral smoothness of the model, which, however, does not imply that the final model would not be less meaningful geologically, since the final model explains two independent data sets. In other words, as the final results are constrained by the 3D gravity model, they not only allow better density models but also give a geologically more coherent and smoother model without increasing considerably the data

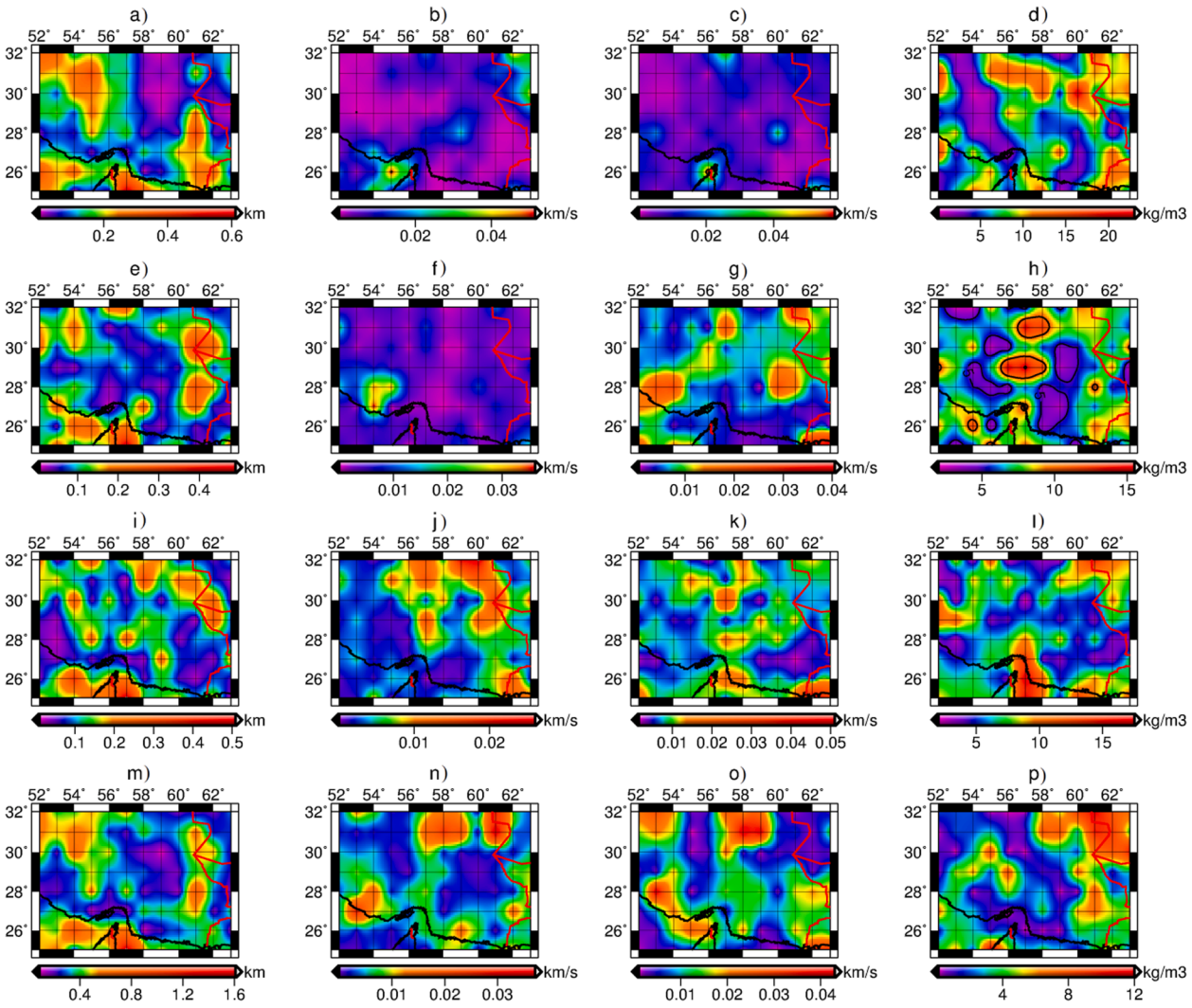

Fig. 14. Maps of uncertainty distribution in the model parameters after the second round of SA modeling: (a) Thickness of sediments (km), (b) Vs of the sediment layer (km/s), (c) Vp of the sediment layer (km/s), (d) Density of the sediments (kg/m^3), (e) Thickness of upper crust (km), (f) Vs of upper crust (km/s), (g) Vp of upper crust (km/s), (h) Density of upper crust (kg/m^3), (i) Thickness of lower crust(km), (j) Vs of lower crust (km/s), (k) Vp of lower crust (km/s), (l) Density of lower crust (kg/m^3), (m) Moho depth (km), (n) Vs of mantle lithosphere (km/s), (o) Vp of mantle lithosphere (km/s), and (p) Density of mantle lithosphere (kg/m^3).

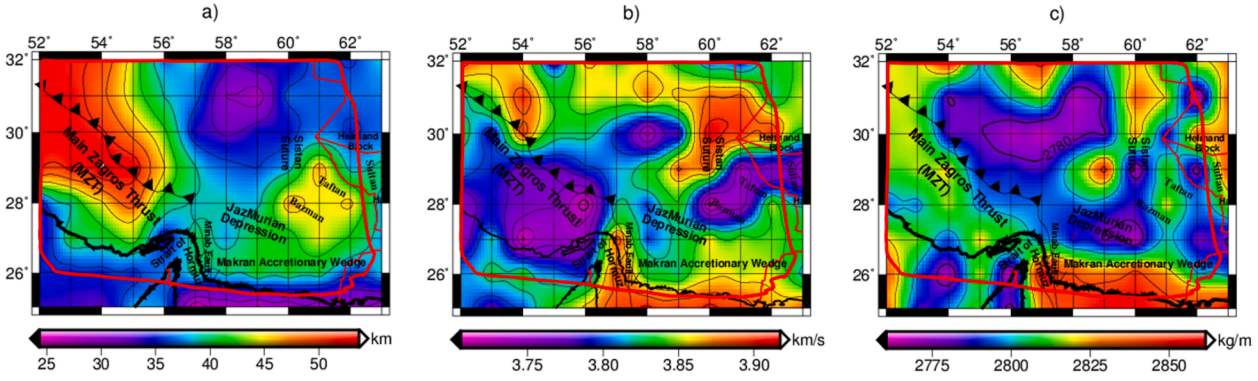

Fig. 15. Final crustal model based of real data. (a) Moho depth (km), (b) The average crustal shear wave velocity (km/s), and (c) The average crustal density (kg/m3). The areas with appropriate resolution has been marked by a red contour.

misfit (Fig. 12). As explained by Mohammadi (2020), Rayleigh wave group velocity tomography has low resolution in the east and south of the region. Therefore, as we expected, our data misfits are larger in these parts of the region (Figs. 9 and 13). In order to see the crustal structures, the Moho depth, average crustal shear wave velocity and average crustal density for the region are shown in Fig. 15. Furthermore, the borders of the areas with acceptable resolution has been marked by a red contour and as we expected data misfit are smaller in these parts of the region.

As mentioned above, the Iranian plateau today is characterized by diverse tectonic domains, including continental collision (Zagros) and subduction of ocean plate (Makran subduction zone). In Makran, our results show the sediment thickness increases from about 4.5–6.5 km to more than 8–9.5 km from the front of the Makran wedge to near the coast (Fig. 12a). Therefore, our results are in a good agreement with the previous studies by Dolati (2010) and Kopp et al. (2000). They found that sediment thickness is 4–7 km in front of the Makran wedge and even more than 10 km near the coastline based on the wide-angle seismic velocity model of offshore Makran.

Many of the prominent features in our results are consistent with the known geological structures. The Strait of Hormuz is considered a transition between the Zagros collision and the Makran oceanic subduction (Regard et al., 2010). A sharp transition boundary between the low- and high-velocity zones with a N-S trend is found across the Minab fault system (see Fig. 12f, 12 g, 12j, 12 k, and especially 12 m) which is considered to represent the boundary between the continental collision zone between Eurasia and Arabia to the west and the oceanic subduction between Eurasia and the Oman Sea to the east (White and Ross, 1979).

In the final results, as can be observed, the northern part of Oman Gulf is characterized by a Moho depth of about 24–30 km increasing northward towards the Iranian coast to 34–42 km (Fig. 12m). The Moho deepening continues northward to reach its maximum value of about 47–49 km, where the subducting plate bends below the Taftan-Bazman volcanic arc (Fig. 12m). The significantly deeper part of the Moho is concentrated around the Taftan volcano which is compatible with earlier studies in the region (Niazi et al., 1980; Kopp et al., 2000; Dehghani and Makris, 1984; Jiménez-Munt et al., 2012; Smith et al., 2013; Entezar-Saadat et al., 2017; Abdollahi et al., 2018; Abdollahi et al., 2019). Also, our results give a Moho depth beneath the Main Zagros Thrust of 50–58 km that is consistent with earlier researches (e.g. Dehghani and Makris, 1984; Shad Manaman et al., 2011; Abdollahi et al., 2018; Abdollahi et al., 2019).

The shear and compressional velocity images of the upper-mantle structure across the Makran subduction zone (Fig. 12n and 12o) depict a high-velocity anomaly under the north of Oman seafloor which continues under the entire zone of Makran belt. The location of the high shear (compressional) velocity anomaly within the Oman Sea and the occurrence of a low velocity anomaly northwards inland represent the subducting slab in the south and the beginning of the mantle wedge in the north. This is also consistent with previous studies that suggested subduction of the high-velocity slab of the Arabian plate northwards (e.g., Shad Manaman et al., 2011; Abdollahi et al., 2018; Abdollahi et al., 2019). In addition, our results show a high shear and compressional velocity anomaly in the upper mantle beneath Zagros (Fig. 10n and 10o).

The average shear velocity images of the crust display high S-wave velocities under the northern part of Oman Gulf. The crust under the forearc, volcanic arc and backarc settings of Makran subduction zone is characterized by lower-velocities (see Fig. 12f, 12j).

The density image of the region shows a high density anomaly in the upper-mantle under the Main Zagros Thrust and the Gulf of Oman, which is decreasing northward to Makran. Furthermore, the high density in the upper-mantle of Makran, found in the same area as the high upper-mantle velocities, indicates the subducting slab and its corresponding density increase.

5. Conclusions

Based on cooperative inversion of Rayleigh wave group velocities and free-air gravity data, we constructed a model of crustal and uppermost mantle P and S wave velocity and density distributions. The main results are summarized as follows:

- The Makran area is characterized by a Moho depth of about 24–30 km in the southern, oceanic part, increasing northward towards the Makran forearc setting to 34–42 km. Further North, Moho depth reaches 47–49 km beneath the Taftan-Bazman volcanic-arc.
- The average crustal density has maximum values of about 2860 kg/m^3 under the oceanic crust of the Gulf of Oman Oman, decreasing northward to the Makran region with about 2760 kg/m^3 indicating a continental crust.
- The results show high shear and compressional velocities under the Gulf of Oman, decreasing to the north of the Makran region.
- In the uppermost mantle, down to 200 km, seismic velocities and densities decrease notably northwards pointing to a thinner lithosphere under the volcanic qrc than under the Oman Sea and the Makran forearc.

Declaration of Competing Interest

The authors declare that they have no known competing financial interests or personal relationships that could have appeared to influence the work reported in this paper.

Acknowledgments

Figures were created with GMT (Wessel and Smith, 1995). Thanks to Bureau Gravimétrique International (BGI) for gravity data. Many thanks to Dr. Najmieh Mohammadi for generously providing us with her Ph.D. research results on the Rayleigh wave dispersion curve data. We are also immensely grateful to Jon B. Fletcher and the anonymous reviewers for their valuable comments on an earlier version of the manuscript.

Appendix A. Supplementary data

Supplementary data to this article can be found online at https://doi.org/10.1016/j.jaesx.2022.100101.

References

Abdollahi, S., Ardestani, V.E., Zeyen, H., Shomali, Z.H., 2018. Crustal and upper mantle structures of Makran subduction zone, SE Iran by combined surface wave velocity analysis and gravity modeling. Tectonophysics 747–748, 191–210. https://doi.org/10.1016/j.tecto.2018.10.005.

Abdollahi, S., Zeyen, H., Ardestani, V.E., Shomali, Z.H., 2019. 3D joint inversion of gravity data and Rayleigh wave group velocities to resolve shear-wave velocity and density structure in the Makran subduction zone, south-east Iran. J. Asian Earth Sci. 173, 275–290. https://doi.org/10.1016/J.JSEAES.2019.01.029.

Agard, P., Monié, P., Gerber, W., Omrani, J., Molinaro, M., Meyer, B., Labrousse, L., Vrielynck, B., Jolivet, L., Yamato, P., 2006. Transient, synobduction exhumation of Zagros blueschists inferred from P-T, deformation, time, and kinematic constraints: Implications for Neotethyan wedge dynamics. J. Geophys. Res. Solid Earth 111 (B11), n/a–n/a. https://doi.org/10.1029/2005JB004103.

Agard, P., Omrani, J., Jolivet, L., Mouthereau, F., 2005. Convergence history across Zagros (Iran): constraints from collisional and earlier deformation. Int. J. Earth Sci. 94 (3), 401–419. https://doi.org/10.1007/s00531-005-0481-4.

Alinaghi, A., Koulakov, I., Thybo, H., 2007. Seismic tomographic imaging of P - and S -waves velocity perturbations in the upper mantle beneath Iran. Geophys. J. Int. 169, 1089–1102. https://doi.org/10.1111/j.1365-246X.2007.03317.x.

Beaty, K.S., Schmitt, D.R., 2003. Repeatability of multimode Rayleigh-wave dispersion studies. GEOPHYSICS 68 (3), 782–790. https://doi.org/10.1190/1.1581031.

Beaty, K.S., Schmitt, D.R., Sacchi, M., 2002. Simulated annealing inversion of multimode Rayleigh wave dispersion curves for geological structure. Geophys. J. Int. 151, 622–631. https://doi.org/10.1046/j.1365-246X.2002.01809.x.

Berberian, M., 1981. Active faulting and tectonics of Iran. pp. 33–69. https://doi.org/10.1029/GD003p0033.

Berberian, M., Yeats, R.S., 2000. Pattern of historical earthquake rupture in the Iranian plateau. B. Seism. Soc. Am. 89, 120–139.

Bucher, R.L., Smith, R.B., 1971. Crustal Structure of the Eastern Basin and Range Province and the Northern Colorado Plateau from Phase Velocities of Rayleigh Waves. The Structure and Physical Properties of the Earth's Crust. J.G. Heacock (Ed.). https://doi.org/10.1029/GM014p0059.

Burg, J.-P., 2018. Geology of the onshore Makran accretionary wedge: Synthesis and tectonic interpretation. Earth-Science Rev. 185, 1210–1231. https://doi.org/10.1016/j.earscirev.2018.09.011.

Byrne, D.E., Sykes, L.R., Davis, D.M., 1992. Great thrust earthquakes and aseismic slip along the plate boundary of the Makran Subduction Zone. J. Geophys. Res. 97 (B1), 449. https://doi.org/10.1029/91JB02165.

Černý, V., 1985. Thermodynamical approach to the traveling salesman problem: An efficient simulation algorithm. J. Optim. Theory Appl. 45 (1), 41–51. https://doi.org/10.1007/BF00940812.
Dehghani, G.A., Makris, J., 1984. The gravity field and crustal structure of Iran. Neues Jahrb. Geol. Palaeontol. Abh. 168 (2-3), 215–229.
Dolati, A., 2010. Stratigraphy, structure geology and low-temperature thermochronology across the Makran accretionary wedge in Iran. Institute of Technology ZURICH, Swiss. PhD thesis.
Entezar-Saadat, V., Motavalli-Anbaran, S.-H., Zeyen, H., 2017. Lithospheric structure of the Eastern Iranian plateau from integrated geophysical modeling: A transect from Makran to the Turan platform. J. Asian Earth Sci. 138, 357–366.
Gallardo-Delgado, L.A., Pérez-Flores, M.A., Gómez-Treviño, E., 2003. A versatile algorithm for joint 3D inversion of gravity and magnetic data. Geophysics 68 (3), 949–959.
Goswami, M., O'connor, K.M., 2007. Comparative assessment of six automatic optimization techniques for calibration of a conceptual rainfall—runoff model. Hydrol. Sci. J. 52 (3), 432–449. https://doi.org/10.1623/hysj.52.3.432.
Herrmann, R.B., 2013. Computer programs in seismology: An evolving tool for instruction and research. Seismol. Res. Lett. 84 (6), 1081–1088.
Herrmann, R.B., Ammon, C.J., 2007. Surface waves, receiver functions and crustal structure, in Computer Programs in Seismology, Version. 3.30.Saint Louis University, Missouri.
Herrmann, R.B., Mitchell, B.J., 1975. Statistical analysis and interpretation of surface-wave anelastic attenuation data for the stable interior of North America. Bull. Seismol. Soc. Am. 65, 1115–1128. https://doi.org/10.1785/BSSA0650051115.
Iglesias, A., Cruz-Atienza, V.M., M. Shapiro, N., K. Singh, S., F. Pacheco, J., 2001. Crustal structure of south-central Mexico estimated from the inversion of surface-wave dispersion curves using genetic and simulated annealing algorithms. Geofísica Int. 40, 181–190. https://doi.org/10.22201/igeof.00167169p.2001.40.3.321.
Jiménez-Munt, I., Fernàndez, M., Saura, E., Vergés, J., Garcia-Castellanos, D., 2012. 3-D lithospheric structure and regional/residual Bouguer anomalies in the Arabia-Eurasia collision (Iran). Geophys. J. Int. 190, 1311–1324. https://doi.org/10.1111/j.1365-246X.2012.05580.x.
Julia, J., Ammon, C.J., Herrmann, R.B., Correig, A.M., 2000. Joint inversion of receiver function and surface wave dispersion observations. Geophys. J. Int. 143, 99–112.
Kaviani, A., Paul, A., Bourova, E., Hatzfeld, D., Pedersen, H., Mokhtari, M., 2007. A strong seismic velocity contrast in the shallow mantle across the Zagros collision zone (Iran). Geophys. J. Int. 171, 399–410. https://doi.org/10.1111/j.1365-246X.2007.03535.x.
Kirkpatrick, S., Gelatt, C.D., Vecchi, M.P., 1983. Optimization by Simulated Annealing. Science (80-. 220 (4598), 671–680.
Koop, W.J., Stoneley, R., 1982. Subsidence history of the Middle East Zagros Basin, Permian to Recent. Philos. Trans. R. Soc. London. Ser. A. Math. Phys. Sci. 305, 149–168. https://doi.org/10.1098/rsta.1982.0031.
Kopp, C., Fruehn, J., Flueh, E.R., Reichert, C., Kukowski, N., Bialas, J., Klaeschen, D., 2000. Structure of the makran subduction zone from wide-angle and reflection seismic data. Tectonophysics 329 (1-4), 171–191.
Lachenbruch, A.H., Morgan, P., 1990. Continental extension, magmatism and elevation; formal relations and rules of thumb. Tectonophysics 174 (1-2), 39–62.
Laske, G., Masters, G., 2013. Update on CRUST1. 0 - A 1-degree global model of Earth's crust. EGU Gen. Assem. 2013 15, 2658.
Lu, Y., Peng, S., Du, W., Zhang, X., Ma, Z., Lin, P., 2016. Rayleigh wave inversion using heat-bath simulated annealing algorithm. J. Appl. Geophys. 134, 267–280. https://doi.org/10.1016/j.jappgeo.2016.09.008.
Menke, W., 2012. Geophysical Data Analysis: Discrete Inverse Theory. Academic Press, London.
Minshull, T.A., White, R.S., Barton, P.J., Collier, J.S., 1992. Deformation at plate boundaries around the Gulf of Oman. Mar. Geol. 104 (1-4), 265–277.
Mitchell, B.J., Herrmann, R.B., 1979. Shear velocity structure in the Eastern United States from the inversion of surface-wave group and phase velocities. Bull. Seismol. Soc. Am. 69, 1133–1148. https://doi.org/10.1785/BSSA0690041133.
Mohammadi, N., 2020. Simultaneous tomography of surface wave periods in estimation of 3D structure of shear wave velocity and attenuation in the Zagros lithosphere. PhD thesis, Institute of Geophysics, University of Tehran, Iran.
Mohammadi, N., Gholami, A., Rahimi, H., Aoudia, A., 2020. Simultaneous tomography of all periods in surface wave analysis. Phys. Earth Planet. Inter. 298, 106338. https://doi.org/10.1016/j.pepi.2019.106338.
Mokhtari, M., Ala Amjadi, A., Mahshadnia, L., Rafizadeh, M., 2019. A review of the seismotectonics of the Makran Subduction Zone as a baseline for Tsunami Hazard Assessments. Geosci. Lett. 6, 13. https://doi.org/10.1186/s40562-019-0143-1.
Molinari, I., Morelli, A., 2011. EPcrust: a reference crustal model for the European Plate. Geophys. J. Int. 185 (1), 352–364.
Monié, P., Agard, P., 2009. Coeval blueschist exhumation along thousands of kilometers: Implications for subduction channel processes. Geochemistry, Geophys. Geosystems 10 (7), n/a–n/a. https://doi.org/10.1029/2009GC002428.
Motaghi, K., Tatar, M., Priestley, K., Romanelli, F., Doglioni, C., Panza, G.F., 2015. The deep structure of the Iranian Plateau. Gondwana Res. 28 (1), 407–418. https://doi.org/10.1016/j.gr.2014.04.009.
Niazi, M., Shimamura, H., Matsu'ura, M., 1980. Microearthquakes and crustal structure off the Makran Coast of Iran. Geophys. Res. Lett. 7 (5), 297–300.
Pei, D., Louie, J.N., Pullammanappallil, S.K., 2008. Improvements on Computation of Phase Velocities of Rayleigh Waves Based on the Generalized R/T Coefficient Method. Bull. Seismol. Soc. Am. 98 (1), 280–287. https://doi.org/10.1785/0120070057.
Penney, C., Tavakoli, F., Saadat, A., Nankali, H.R., Sedighi, M., Khorrami, F., Sobouti, F., Rafi, Z., Copley, A., Jackson, J., Priestley, K., 2017. Megathrust and accretionary wedge properties and behaviour in the Makran subduction zone. Geophys. J. Int. 209, 1800–1830. https://doi.org/10.1093/gji/ggx126.
Platt, J.P., Leggett, J.K., Alam, S., 1988. Slip vectors and fault mechanics in the Makran Accretionary Wedge, southwest Pakistan. J. Geophys. Res. 93 (B7), 7955. https://doi.org/10.1029/JB093iB07p07955.
Platt, J.P., Leggett, J.K., Young, J., Raza, H., Alam, S., 1985. Large-scale sediment underplating in the Makran accretionary prism, southwest Pakistan. Geology 13 (7), 507. https://doi.org/10.1130/0091-7613(1985)13<507:LSUITM>2.0.CO;2.
Quittmeyer, R.C., Jacob, K.H., 1979. Historical and modern seismicity of Pakistan, Afghanistan, northwestern India, and southeastern Iran. Bull. Seismol. Soc. Am. 69, 773–823.
Rahimi, H., Hamzehloo, H., Vaccari, F., Panza, G.F., 2014. Shear-Wave Velocity Tomography of the Lithosphere-Asthenosphere System beneath the Iranian Plateau. Bull. Seismol. Soc. Am. 104 (6), 2782–2798. https://doi.org/10.1785/0120130319.
Rashidi, A., Dutykh, D., Shomali, Z.H., Keshavarz Farajkhah, N., Nouri, M., 2020. A Review of Tsunami Hazards in the Makran Subduction Zone. Geosciences 10, 372. https://doi.org/10.3390/geosciences10090372.
Regard, V., Hatzfeld, D., Molinaro, M., Aubourg, C., Bayer, R., Bellier, O., Yamini-Fard, F., Peyret, M., Abbassi, M., 2010. The transition between Makran subduction and the Zagros collision: recent advances in its structure and active deformation. Geol. Soc. London. Spec. Publ. 330 (1), 43–64.
Ryden, N., Park, C.B., 2006. Fast simulated annealing inversion of surface waves on pavement using phase-velocity spectra. GEOPHYSICS 71 (4), R49–R58. https://doi.org/10.1190/1.2204964.
Manaman, N.S., Shomali, H., Koyi, H., 2011. New constraints on upper-mantle S-velocity structure and crustal thickness of the Iranian plateau using partitioned waveform inversion. Geophys. J. Int. 184 (1), 247–267.
Shapiro, N.M., Ritzwoller, M.H., 2002. Monte-Carlo inversion for a global shear-velocity model of the crust and upper mantle. Geophys. J. Int. 151, 88–105. https://doi.org/10.1046/j.1365-246X.2002.01742.x.
Shirzad, T., Riahi, M.-A., Assumpção, M.S., 2019. Crustal Structure of the Collision-Subduction Zone in South of Iran Using Virtual Seismometers. Sci. Rep. 9, 10851. https://doi.org/10.1038/s41598-019-47430-y.
Smith, G.L., McNeill, L.C., Wang, K., He, J., Henstock, T.J., 2013. Thermal structure and megathrust seismogenic potential of the Makran subduction zone. Geophys. Res. Lett. 40 (8), 1528–1533.
Taghizadeh-Farahmand, F., Afsari, N., Sodoudi, F., 2014. Crustal thickness of Iran inferred from converted waves. Pure Appl. Geophys. 172 (2), 309–331.
Tirrul, R., Bell, I.R., Griffis, R.J., Camp, V.E., 1983. The Sistan suture zone of eastern Iran. Geol. Soc. Am. Bull. 94 (1), 134. https://doi.org/10.1130/0016-7606(1983)94<134:TSSZOE>2.0.CO;2.
Vernant, P., Nilforoushan, F., Hatzfeld, D., Abbassi, M.R., Vigny, C., Masson, F., Nankali, H., Martinod, J., Ashtiani, A., Bayer, R., Tavakoli, F., Chéry, J., 2004. Present-day crustal deformation and plate kinematics in the Middle East constrained by GPS measurements in Iran and northern Oman. Geophys. J. Int. 157, 381–398. https://doi.org/10.1111/j.1365-246X.2004.02222.x.
White, R.S., Louden, K.E., 1982. The Makran continental margin; structure of a thickly sedimented convergent plate boundary. Studies in continental margin geology. S. Watkins Joel L. Drake Charles. Tulsa, OK, United States. Am. Assoc. Pet. Geol. 34, 499–518.
White, R.S., Ross, D.A., 1979. Tectonics of the Western Gulf of Oman. J. Geophys. Res. 84 (B7), 3479–3489.
Yamanaka, H., Ishida, H., 1996. Application of genetic algorithms to an inversion of surface-wave dispersion data. Bull. Seismol. Soc. Am. 86, 436–444. https://doi.org/10.1785/BSSA0860020436.
Zeyen, H., Ayarza, P., Fernàndez, M., Rimi, A., 2005. Lithospheric structure under the western African-European plate boundary: A transect across the Atlas Mountains and the Gulf of Cadiz. Tectonics 24 (2), n/a–n/a.
Zeyen, H., Pous, J., 1993. 3-D joint inversion of magnetic and gravimetric data with a priori information. Geophys. J. Int. 112 (2), 244–256.